ERDC SR-23-11

US Army Corps of Engineers®
Engineer Research and Development Center

ERDC
ENGINEER RESEARCH & DEVELOPMENT CENTER

Establishing a Series of Dust Event Case Studies for East Asia

Theodore W. Letcher, Kent H. Sparrow, and Sandra L. LeGrand

October 2023

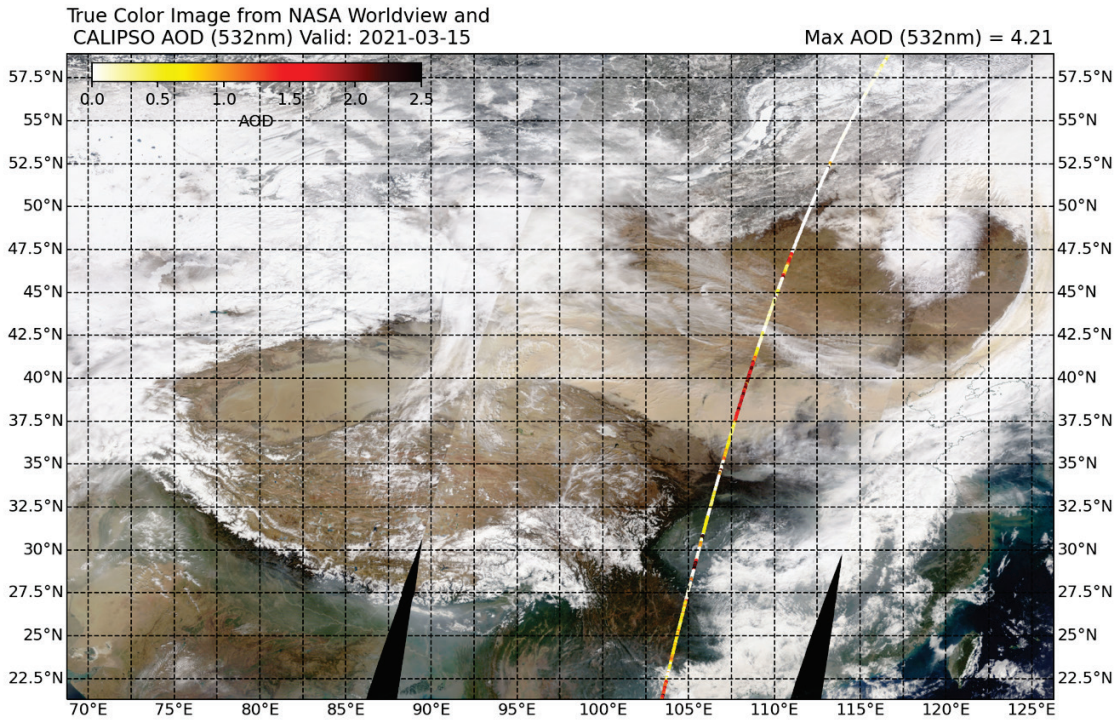

Engineer Research and Development Center

The US Army Engineer Research and Development Center (ERDC) solves the nation's toughest engineering and environmental challenges. ERDC develops innovative solutions in civil and military engineering, geospatial sciences, water resources, and environmental sciences for the Army, the Department of Defense, civilian agencies, and our nation's public good. Find out more at www.erdc.usace.army.mil.

To search for other technical reports published by ERDC, visit the ERDC online library at https://erdclibrary.on.worldcat.org/discovery.

ERDC SR-23-11
October 2023

Establishing a Series of Dust Event Case Studies for East Asia

Theodore W. Letcher

US Army Engineer Research and Development Center (ERDC)
Cold Regions Research and Engineering Laboratory (CRREL)
72 Lyme Road
Hanover, NH 03755-1290

Kent H. Sparrow and Sandra L. LeGrand

US Army Engineer Research and Development Center (ERDC)
Geospatial Research Laboratory (GRL)
7701 Telegraph Road
Alexandria, VA 22315-3864

Final Special Report (SR)

Prepared for Air Force Lifecycle Management Center
75 Vandenburg Drive, Building 1630
Hanscom AFB, MA 01731-2103

Under MIPR F28DAN2070G001

Abstract

Dust aerosols have a wide range of effects on air quality, health, land-management decisions, aircraft operations, and sensor data interpretations. Therefore, the accurate simulation of dust plume initiation and transport is a priority for operational weather centers. Recent advancements have improved the performance of dust prediction models, but substantial capability gaps remain when forecasting the specific location and timing of individual dust events, especially extreme dust outbreaks. Operational weather forecasters and US Army Engineer Research and Development Center (ERDC) researchers established a series of reference case study events to enhance dust transport model evaluation. These reference case studies support research to improve modeled dust simulations, including efforts to increase simulation accuracy on when and where dust is lofted off the ground, dust aerosols transport, and dust-induced adverse air quality issues create hazardous conditions downstream. Here, we provide detailed assessments of four dust events for Central and East Asia. We describe the dust-event lifecycle from onset to end (or when dust transports beyond the area of interest) and the synoptic and mesoscale environmental conditions governing the process. Analyses of hourly reanalysis data, spaceborne lidar and aerosol optical depth retrievals, upper-air soundings, true-color satellite imagery, and dust-enhanced false-color imagery supplement the discussions.

Contents

Figures

Preface

This study was conducted for the Air Force Lifecycle Management Center under the Enhanced Dust Emission Characterization for Improved Atmospheric Dust Forecasting project, MIPR F28DAN2070G001.

The work was performed by the Terrestrial and Cryospheric Sciences Branch of the Research and Engineering Division, US Army Engineer Research and Development Center, Cold Regions Research and Engineering Laboratory (ERDC-CRREL). At the time of publication, Dr. John Weatherly was branch and acting division chief. Dr. Ivan P. Beckman was deputy director of ERDC-CRREL, and Dr. Joseph L. Corriveau was director.

The Information Generation and Management Branch of the Geospatial Research Division, ERDC Geospatial Research Laboratory (ERDC-GRL), also performed this work. At the time of publication of this report, Mr. Michael F. Mailloux was branch chief, and Mr. Jeffrey B. Murphy was division chief. The deputy director of the ERDC-GRL was Ms. Valerie L. Carney, and the director was Mr. David R. Hibner.

COL Christian Patterson was commander of ERDC, and the director was Dr. David W. Pittman.

This page intentionally left blank.

1 Introduction

1.1 Background

Dust aerosols have a wide range of effects on air quality, health, land-management decisions, aircraft operations, and sensor data interpretations (Department of the Army 2019, 2020, 2021; Goudie and Middleton 2006; Miri et al. 2009; Baddock et al. 2013; Tozer and Leys 2013; Gonzalez-Martin et al. 2014; Middleton 2017; Vergadi et al. 2022; Zilberman and Kopeika 2022). Accordingly, accurate simulation of dust plume initiation and transport is a priority for mission planning and operational weather centers (Knippertz and Stuut 2014; Sprigg et al. 2014; Shepherd et al. 2016; Joint Chiefs of Staff 2018). While recent advancements have improved the general performance of dust prediction models (e.g., Chen et al. 2022; Zhao et al. 2022), capability gaps in simulating the specific location and timing of individual dust events, especially extreme dust outbreaks, continue to be a challenge (LeGrand and Brooks 2018; Richter and Gill 2018; Alter et al. 2022).

To help resolve these issues, researchers from the US Army Engineer Research and Development Center (ERDC) are working to establish a series of thoroughly documented case studies to support dust transport model evaluation and validation activities (Gallagher et al. 2022; Alter et al. 2022; Sparrow and LeGrand 2023). As part of the evaluation process, developers must establish how well the model recreated the forcing conditions, including the synoptic evolution, storm progression, vertical structure, associated precipitation patterns (if any), and surface wind fields, associated with the simulated dust event under consideration. This particular step is critical for discerning errors in the environmental forcing conditions driving the dust event and issues with dust parameterization.

This report provides detailed analyses of four dust events that originated in Central and East Asia. East Asian dust events with hazardous air quality conditions that disrupt transportation, agriculture, and communication primarily occur during the spring months (Jin et al. 2022; Rogowski et al. 2021; Zhang et al. 2018). These events typically originate from the prominent dust source regions of East Asia, which primarily consist of the Gobi and Taklamakan Deserts, the Hexi Corridor, and the Alxa Desert (Huang et al. 2014; Zhou et al. 2019; Bao et al. 2022).

1.2 Objective

The objective of this study was to document the environmental forcing conditions and storm evolution of four extreme dust events in the Central and East Asia regions, including storms that ranged from large-scale, synoptically driven dust plumes to mesoscale *haboob** events. Each event description provides in-depth analyses of data from reanalysis products, surface observations, remotely sensed parameters, and satellite imagery to form a clear description of the forcing environment from the initiation to the dissipation of each dust plume. The information documented in this report supports ongoing dust modeling validation efforts within ERDC.

1.3 Approach

This study focused on four events that occurred across Central and East Asia, spanning a range of different regions and dust storm morphologies, including

1. a widespread, synoptically driven dust storm that occurred in conjunction with a strong midlatitude cyclone between 13 and 20 March 2021;
2. a short-lived convective dust event that occurred along an outflow boundary in the Gansu province east of the Taklamakan Desert on 25 July 2021;
3. a powerful, but short-lived, event that occurred in Kazakhstan and Uzbekistan on 4–5 November 2021, following a cold frontal passage that interacted with regional topography; and
4. a widespread synoptic event, similar to the 13–20 March 2021 event, that occurred between 1 and 7 May 2017.

Figure 1 presents an overview of the geographic region and annotations illustrating each event.

* Italicized terms are defined in the glossary, which can be found in the Appendix.

Figure 1. Annotated overview illustrating the approximate geographic progression of each of the four dust events. (Map image is the intellectual property of Esri and is used herein under license. Copyright 2020 Esri and its licensors. All rights reserved.)

For each event, we interpreted available weather data to describe the general synoptic, *mesoscale*, and local environmental forcing conditions that governed dust storm evolution. In particular, we used gridded reanalysis data from the European Center for Medium-Range Weather Forecasting's (ECMWF) reanalysis product, ERA5. This dataset optimally combines calibrated output from the ECMWF Integrated Forecasting System model with available in situ and remote sensing observations to provide a "best-guess" representation of the global atmospheric configuration. The primary advantage of this dataset is that it provides a continuous gridded dataset with global coverage that includes important dynamic, kinematic, and thermodynamic variables at numerous atmospheric levels. These data are necessary for identifying key upper-level synoptic and surface meteorological drivers associated with each dust event. The ECMWF ERA5 product was particularly important for this assessment because large regions of East Asia, especially the dust source regions, are otherwise data sparse.

In addition to the ERA5 dataset, our weather and dust analyses incorporated information derived from spaceborne remote sensing collections. We primarily used data from three different satellite platforms.

First, we used available operational satellite imagery from the Meteosat Second Generation Spinning Enhanced Visible and InfraRed Imager

(MSG-SEVIRI) to help identify synoptic and mesoscale weather features and dust plumes. Specifically, we used the regional false-color, dust-enhanced imagery "pink dust" product provided by the Met Office. A key advantage of MSG-SEVIRI is that it is in geostationary orbit with good coverage of East Asia and provides continuous monitoring of the region.

In addition to MSG-SEVIRI, we used true-color imagery from the Moderate Resolution Imaging Spectroradiometer (MODIS) onboard the Aqua and Terra satellites and imagery from the newer Visible Infrared Imaging Radiometer Suite (VIIRS) satellite to help identify dust source regions. As polar orbiting satellites, they do not provide continuous coverage like MSG-SEVIRI. However, they provide spatially detailed, high-resolution information from daily composites.

Finally, we used post-processed lidar data from the Cloud-Aerosol Lidar and Infrared Pathfinder Satellite Observation (CALIPSO) satellite. While these data have very limited spatial coverage due to the relatively small footprint of the lidar beam, they provide detailed information regarding the vertical extent and intensity of dust plumes when the satellite overpass coincides with them. However, coincident overpasses are sporadic, and therefore, data from the CALIPSO platform were not available or useful for all cases.

While sparse, we used other traditional meteorological observations, such as surface weather and upper-air (i.e., weather balloon) data, when they were available. Section 2 provides detailed information on each of these data products.

2 Methodology

We analyzed environmental forcing conditions and dust storm evolution using data from the ERA5 reanalysis dataset, MODIS, MSG-SEVIRI, and CALIPSO. Analysts down selected the four events from an inventory of potential options that were identified by reviewing published literature, news articles, and social media posts. When selecting the final four events, we considered the likely atmospheric features and scales involved (e.g., synoptic versus mesoscale), geographic location, societal impact, and data availability. Sections 2.1–2.8 describe the analysis data used for this study.

2.1 Meteosat Second Generation Spinning Enhanced Visible and InfraRed Imager (MSG-SEVIRI) Dust-Enhanced False-Color Imagery

We used dust-enhanced false-color "pink dust" imagery derived from the Spinning Enhanced Visible InfraRed Imager (SEVIRI) onboard the geostationary Meteosat Second Generation (MSG) satellite generated by the Met Office to highlight the initiation and transport of dust plumes. These images are useful for analyzing the evolution of dust events because the false-color scheme can help distinguish dust from other meteorological and geographic features (Banks and Brindley 2013; Brindley et al. 2012). In this imagery, thick clouds often display a deep red color, while dust typically has a bright pink appearance (Sinclair and Jones 2017). The data are viewable at a 1 km* resolution and are most useful for analyzing dust events that occur over Europe, Africa, and the Middle East. We were only able to use MSG-SEVIRI data for three of our four case studies because the Met Office data archive did not extend back far enough in time to encompass the May 2017 time period.

There are important limitations to consider when reviewing dust transport events with satellite imagery, especially when the dust aerosols are near their point of origin or cross over barren and sparsely vegetated landscapes (Sinclair and LeGrand 2019; Walker et al. 2009). In general, there must be sufficient thermal and reflectance contrast signals between the dust and the underlying land surface for the algorithms or interpreter to

* For a full list of the spelled-out forms of the units of measure used in this document, please refer to *US Government Publishing Office Style Manual*, 31st ed. (Washington, DC: US Government Publishing Office, 2016), 248–252, https://www.govinfo.gov/content/pkg/GPO-STYLEMANUAL-2016/pdf/GPO-STYLEMANUAL-2016.pdf.

discern the presence of dust. As such, dust aerosols near their deflating source may not be readily visible in the satellite imagery. The dust may have experienced several kilometers of downwind advection prior to satellite detection. Accordingly, satellite imagery is not necessarily a reliable resource for pinpointing the exact location of dust emission beyond a generalized source region.

2.2 ERA5 Reanalysis Data

We used the ERA5 dataset (Hersbach et al. 2020) to analyze synoptic and mesoscale meteorological conditions for each dust event. This dataset, which is produced by the ECMWF, provides hourly data with 30 km horizontal grid spacing at 37 pressure levels, ranging from the surface to 0.01 hPa. The dataset also consists of atmospheric variables at various critical levels, such as 2 m *dewpoint* temperature, mean sea-level pressure (MSLP), and 2 m temperature, that are commonly used for analyzing weather conditions. The time period of available hourly data ranges from 1950 to present.

The ERA5 data analyzed in this study included the variables that follow:

1. *Geopotential heights* at 300, 500, and 850 hPa pressure levels. Analysts commonly use geopotential height to assess upper-air weather and circulation patterns and to identify high- and low-pressure circulations in the atmosphere.
2. U (zonal; west to east) and V (meridional; south to north) wind vector components at 300 and 850 hPa pressure levels. Upper level (i.e., 300 hPa) wind analyses are useful for highlighting jet-streak winds that set the environment for surface *cyclogenesis*. We reviewed low-level (i.e., 850 hPa) winds to identify frontal systems and strong boundary layer winds that could potentially extend down toward the land surface (creating strong wind flow conditions favorable for dust production).
3. *Vorticity* at the 500 hPa pressure level. Weather forecasters commonly use the 500 hPa vorticity field to identify large-scale upper-level circulations associated with midlatitude and tropical cyclones.
4. Temperature at the 850 hPa pressure level. Temperatures at this level are useful for identifying frontal systems and different air masses.
5. MSLP. MSLP patterns help to identify the location and strength of cyclones that can create favorable conditions for dust initiation and transport.

6. U and V wind vector components at 10 m above the ground. This information helps identify the surface winds associated with midlatitude cyclones or gust fronts that contribute to dust lofting from the land surface.

Because reanalysis datasets initially derive from numerical model simulations adjusted with observed data, we treated the ERA5 information as a best guess of the atmospheric state. While they are not observations, researchers generally consider reanalysis data to be good indicators of general synoptic and large-scale patterns in data-sparse environments.

2.3 Cloud-Aerosol Lidar and Infrared Pathfinder Satellite Observation (CALIPSO)

The Cloud-Aerosol Lidar with Orthogonal Polarization (CALIOP) is an instrument that is part of CALIPSO. We used data from this instrument to analyze the vertical extent of aerosols present in each event. This instrument measures the extinction of two signals, 1,064 nm (infrared) and 532 nm (visible), as they travel through the atmosphere to estimate atmospheric aerosol profiles using dual polarization-backscatter lidar (Winker et al. 2007). The system includes a combination of passive infrared and visible imagers to diagnose the vertical extent of aerosols and the distribution of various aerosol types (e.g., dust, smoke, and ash; Liu et al. 2008, 2012; He and Yi 2015).

Data providers also use the extinction values recorded by CALIPSO to estimate transects of total column *aerosol optical depth* (AOD) along the sensor path. AOD is a wavelength-dependent, unitless value that indicates the degree to which aerosols prevent the transmission of light (or, depending on the wavelength, signal) through the atmosphere. In clear sky conditions, AOD values are usually ≤0.1, while in poor air quality conditions, AOD values may be much higher, ranging from 0.5 to >4.0. However, specific AOD values will vary depending on factors such as the speciation, size distribution, and number of aerosols present in the air; the location under consideration; and the time of day. For dusty conditions, AOD values tend to range from 0.1 to 3.0 or higher, with the highest values associated with the thickest and most extensive dust plumes. In general, AOD values greater than 1.0 indicate notably reduced visibility conditions, and values greater than 3.0 tend to align with extreme visibility issues.

2.4 Moderate Resolution Imaging Spectroradiometer (MODIS) Monthly Mean Snow Cover Fraction

We reviewed the monthly mean snow cover fraction for certain cases using the MODIS level 3 snow cover fraction product (MOD10CM; Hall and Riggs 2021b). This dataset provides estimates of monthly snow cover fraction on a 0.05° resolution global grid using input from the MOD10A1 snow cover product, a dataset derived using the normalized snow difference index (Hall and Riggs 2021a).

2.5 True-Color Imagery from NASA Worldview

The NASA Earth Observing System Data and Information System Worldview v4.2.0 interactive web interface (NASA, n.d.) provides a streamlined capability to access true-color imagery from the MODIS level 1B calibrated radiances product onboard both the Aqua and Terra satellites (MCST 2017) and data from the VIIRSVJ103MOD_NRT product (Wolfe et al. 2013). These image collections provide relatively high-resolution (i.e., 250 m for MODIS; 375 m resampled to 250 m grid spacing for VIIRS) daily composite satellite imagery for qualitative assessment of each event. In particular, we found the true-color imagery helpful for subjectively assessing cloud features and the position and relative origin of dust plumes. Throughout the report, we refer to both sources of true-color composite imagery as "Worldview imagery" to avoid confusion because the platform with the best daily image option available for highlighting dust, surface characteristics, and other atmospheric phenomena varied throughout the study.

Regarding satellite product resolution, we acknowledge that some very narrow, subgrid-scale dust plumes associated with the focus dust events may go undetected. However, given the general scale of the chosen case studies (i.e., mesoscale or coarser) and the widespread nature of the resultant dust hazards, we anticipated that both the MODIS and VIIRS products would be of sufficient resolution to illustrate the general patterns of dust aerosol transport. As discussed previously, higher resolution imagery does not always guarantee better outcomes with respect to dust source detection. Accordingly, we anticipated that the minor differences in the original grid resolution between the MODIS and VIIRS true-color imagery products would have minimal influence on our qualitative analysis outcomes.

2.6 Hybrid Single-Particle Lagrangian Integrated Trajectory (HYSPLIT) Model Trajectories

The NOAA Hybrid Single-Particle Lagrangian Integrated Trajectory (HYSPLIT) model is a useful tool for estimating air-parcel trajectories and tracer dispersion from atmospheric reanalysis data using a hybrid Eulerian/Lagrangian approach (Stein et al. 2015). HYSPLIT simulations can support several applications, including dust and pollutant transport simulation, exposure risk assessment, and aerosol provenance investigation. In this work, we used HYSPLIT simulations as a supplement for the three *synoptic-scale* case study events to help identify dust source regions by using forward- and back-trajectory analysis of air parcels. We chose not to perform a HYSPLIT simulation for the convective event that occurred on 25 July 2021 due to the event's short duration.

For this assessment, we produced all of our HYSPLIT simulations using the NOAA Real-Time Environmental Applications and Display System (READY) web-based application (Rolph et al. 2017) using atmospheric data from the 0.5° resolution Global Forecast System model final analysis (GFS-FNL) to characterize the atmospheric motions governing the dust aerosol transport. We released simulated tracer particles in the dispersion model from a point that we subjectively deemed as the approximate dust source location for each event and allowed the tracers to propagate for a six-hour period, beginning at the event onset. We then compared tracer locations at various times throughout the HYSPLIT simulation to dust scenes in the Worldview true-color imagery. Accordingly, we assumed that our dust source designations and understanding of the event evolution were plausible if the simulated tracer locations aligned with dust plume patterns seen in the Worldview imagery at the later stages of each event.

2.7 Vertical Profile Data

Vertical profiles provide observations of key atmospheric parameters at different altitudes. The data collection process usually involves releasing a weather balloon, equipped with instruments to measure position, temperature, humidity, air pressure, and wind speed, into the atmosphere. When displayed on a *skew-T log-p diagram*, the data show changes in atmospheric conditions with altitude and can reveal critical atmospheric features, like temperature inversions, convectively unstable atmospheric layers, and wind shear, that are important for storm assessment. The skew-T log-p diagrams often include associated plots called hodographs,

which provide additional information about wind speed and direction at different heights in the atmosphere. By examining the shape and orientation of hodographs in combination with thermodynamic profiles, analysts can determine the degree of atmospheric convective instability, wind shear, convective storm type and motion, and other atmospheric features like low-level jets or frontal passages. For this study, we obtained our sounding data from the University of Wyoming Department of Atmospheric Sciences archive (University of Wyoming, n.d.). We downloaded these data as text files and plotted the skew-T log-P diagrams using the MetPy software package maintained by Unidata (May et al. 2022).

2.8 In Situ Station Data

In situ surface data are useful for assessing sensible weather conditions at the surface. In particular, they provide critical data regarding wind speed and direction, temperature, humidity, precipitation, and visibility. These data can provide insight into how the large-scale atmospheric features affect conditions near the ground. Often, surface observations can further support model validation efforts because these data are typically the most accessible and direct measurements of important near-surface atmospheric variables. Here, we used data from the Integrated Surface Database (ISD; Lott et al. 2001). For this study, we pulled raw ISD data from a public data archive hosted by the National Centers for Environmental Information (n.d.) and decoded the station data following the ISD data user's guide (National Centers for Environmental Information 2018).

3 Event Case Studies

This section offers detailed descriptions of four different dust events. Although we reviewed and considered multiple forms of data in our assessments, the descriptions provided here only review the products and data resources we felt were most important for telling the storm evolution narrative associated with each event. However, we encourage readers interested in using these case study events to support numerical weather and dust transport model evaluations to consider reviewing all of the data sources discussed in Section 2 to ensure their simulations capture the environmental forcing conditions for the whole domain, not just the areas where dust occurred.

3.1 Central China and Gobi Desert, 13–20 March 2021

3.1.1 Event Overview

The rapid development of an intense midlatitude cyclone ahead of an upper-level *trough* traversing along the Mongolia–China border caused widespread dust during 14 to 17 March 2021. Dust primarily emanated from the broad desert region downstream of the western Khangai Mountains in western Central Mongolia. As the storm crossed Mongolia, a strong cold front blew through the area and entrained large quantities of dust that traveled southeast with north-northwesterly winds behind the front.

Dust over northern China persisted for several days after the frontal passage under the influence of an anticyclone that prohibited dust from transporting out of the region. On 20 March 2021, a second cold front associated with a cyclone moving southeast across Northeast China brought sustained northwesterly winds that helped transport lingering dust out of the region. Overall, this dust event caused widespread adverse effects in northern China, reducing air quality and visibility in this region for a prolonged period (Gui et al. 2022). Gui et al. (2022) noted that this event was among the most extreme events ever recorded, both in size and intensity.

At the height of the storm, the dust plume covered nearly 40% of China's land area and generated concentrations of particulate matter ≤10 μm in diameter (PM_{10}) that exceeded 1,000 μg m^{-3}, a value nearly 10 times the permissible PM_{10} limit for air quality standards, in more than 40 cities

(Gui et al. 2022; Filonchyk and Peterson 2022). This particular dust event is the subject of a growing number of academic studies focusing on its meteorological drivers and air quality impacts (Liang et al. 2021; Tu et al. 2022; Filonchyk and Peterson 2022; Gui et al. 2022; Yin et al. 2022). One intriguing aspect of this event is the likelihood that anomalously dry and low snow conditions over Central Mongolia contributed to the event's severity. For example, Gui et al. (2022) used historical ERA5 reanalysis data to illustrate that the dust associated with this event primarily entrained from a region experiencing anomalously warm and dry spring season conditions.

3.1.2 Synoptic Overview

Before examining the atmospheric forcing conditions associated with the 14–20 March 2021 dust storm, we briefly investigated the antecedent anomalous snow-cover conditions discussed by Gui et al. (2022). Figure 2 shows MODIS-derived snow coverage diagnostics for the region, including the mean March snow-covered area fraction (fSCA) for 2021 ($X_{\mathrm{MAR\_2021}}$), the mean March fSCA for the entire 2000–2022 MODIS record (μ_{MAR}), and the standardized anomaly of fSCA over the March 2021 period ($N_{\mathrm{MAR\_2021}}$) determined by

$$N_{\mathrm{MAR\_2021}} = \frac{X_{\mathrm{MAR\_2021}} - \mu_{\mathrm{MAR}}}{\sigma_{\mathrm{MAR}}},$$

where σ_{MAR} is the standard deviation of March fSCA associated with the entire 2000–2022 MODIS data record. This $N_{\mathrm{MAR\_2021}}$ parameter describes the deviation of March 2021 snow cover conditions from normal climatology in terms of standard deviations. For example, a value of –2 for $N_{\mathrm{MAR\_2021}}$ implies the mean March 2021 fSCA was two standard deviations below normal for the March time frame at that given location.

This analysis confirmed that the dust source area was experiencing anomalously low snow cover during the period leading up to the event, with anomalies ranging between approximately 0.75 and 1.25 standard deviations below normal. In particular, the dust source regions immediately south and east of the Khangai Mountains had no snow cover in March, which was uncharacteristic compared to the 22-year MODIS record. While our analysis supported the hypothesis that antecedent snow-covered area (SCA) conditions contributed to the formation of this extreme dust event,

analyses of other factors affecting surface erodible state, like soil moisture, temperature, and composition, are necessary to fully resolve the issue.

Figure 2. Moderate Resolution Imaging Spectroradiometer (MODIS) mean snow-covered area fraction (fSCA) analyses for the month of March, including (*top*) the mean fSCA for March 2021, (*middle*) the mean March fSCA for the 22-year period spanning the MODIS record (2000–2022), and (*bottom*) the standardized anomaly snow cover. The *red polygon* shows a general outline of key dust sources near the Khangai Mountains.

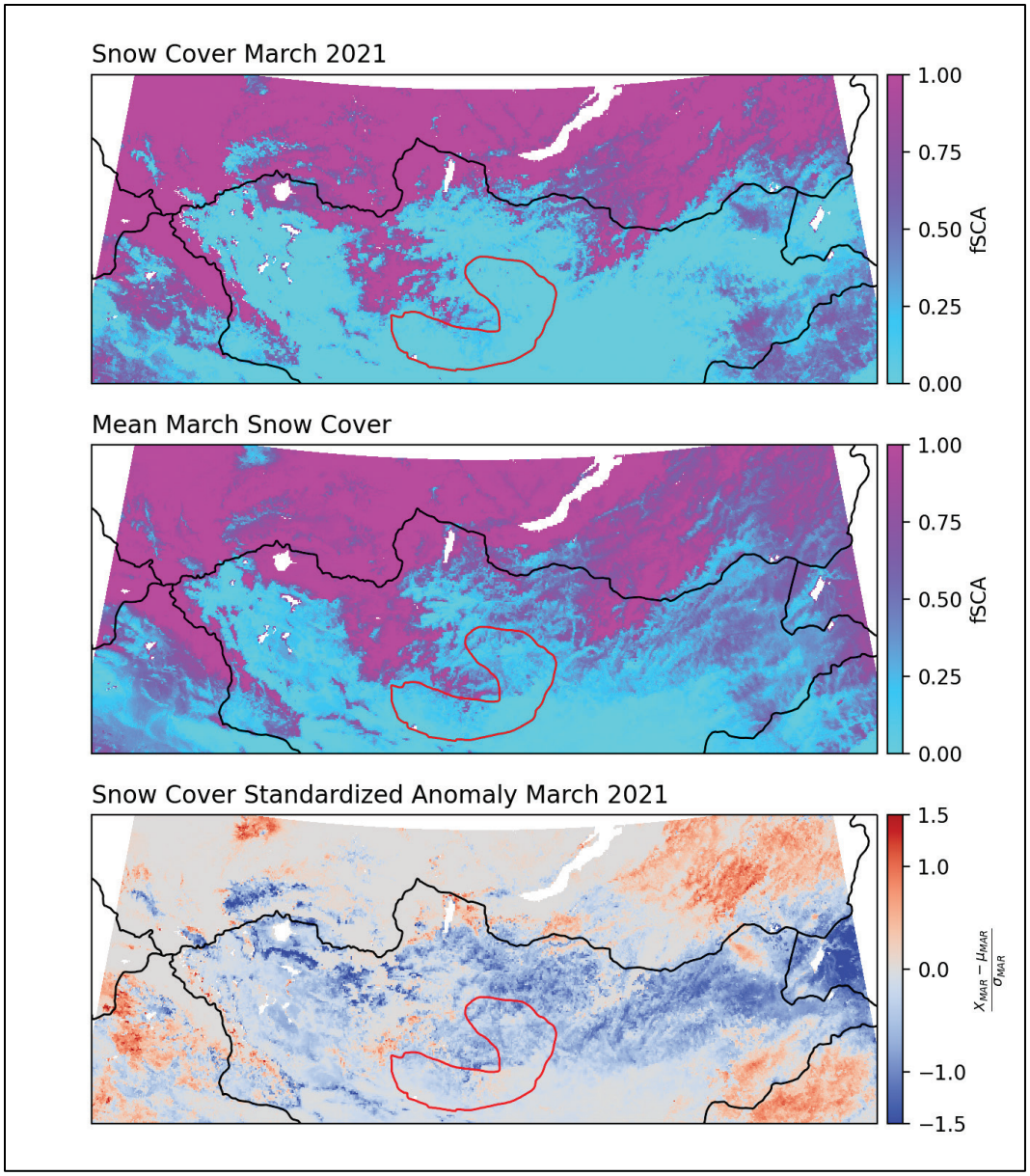

The synoptic evolution of this event followed the typical life cycle of a strong midlatitude cyclone. Here, we first detail the evolution of the event by focusing on the large-scale upper-level synoptic features as they moved across the region. We then investigate the evolution of the mid and lower

troposphere and the synoptic-scale surface features. Finally, we discuss the evolution of the near-surface winds and plausible interactions with the terrain near the dust source regions.

On 12 March 2021 (before the event began), an amplified upper-level trough extended southwest from northern Russia into Kazakhstan (Figure 3*a*). Ahead and south of the trough, the polar jet stream was evident, following a southwest-northeast orientation with an embedded jet streak with peak winds of 85 m s^{-1} extending across Kazakhstan into Southern Russia, near the Mongolian border. Upstream of the 300 hPa trough, a highly amplified blocking *ridge* appeared to be breaking down over Eastern Europe. On 13 March, approximately 20 hours prior to the onset of the dust event, the trough had advanced eastward, and an anticyclonic wave breaking west of the trough facilitated an intensification and a split in the polar jet (Figure 3*b*). This split in the jet stream primed the mid and lower troposphere for rapid cyclogenesis east of the upper-level trough axis. Specifically, the poleward exit region of the southern *jet streak* and the *equatorial entrance region* of the northern jet streak constructively interfered to facilitate upper-level *divergence* and low-level cyclogenesis. By 1200 UTC on 14 March 2021, during and near the end of the dust emission event, the trough had progressed east of the region, and by 1200 UTC on 15 March, a broad area of upper-level high pressure moved in and presided over much of Mongolia and northern China (not shown). The upper-level pattern remained largely quiescent until 19 March 2021, when a second trough crossed the region, bringing another midlatitude cyclone and cold front that cleared any lingering dust from the region.

Figure 3. The 300 hPa heights and winds illustrating the precursor upper-level dynamics approximately (*left*) 48 hours and (*right*) 24 hours ahead of the event. Important features are annotated on the figure. The *blue dot* indicates the approximate location of the main dust source.

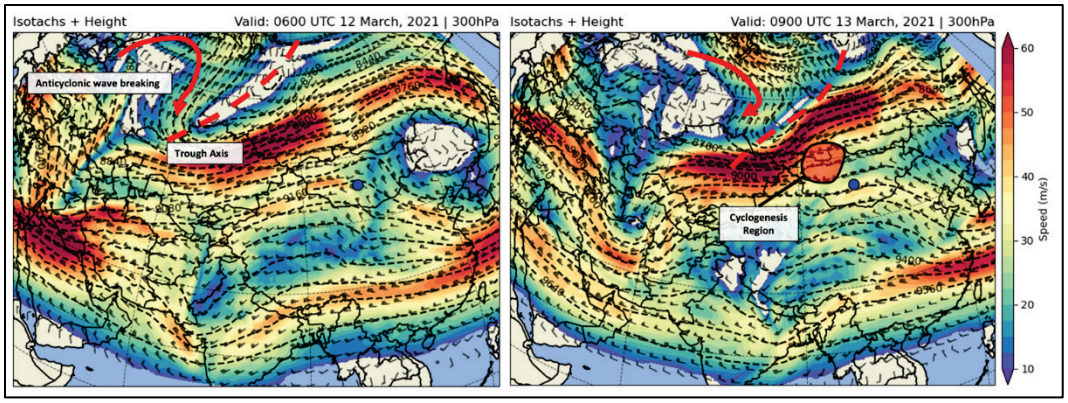

At 1800 UTC on 13 March 2021, the storm was undergoing rapid cyclogenesis as the strengthening cold front approached the dust source region. Figure 4 illustrates this process and other storm dynamics at various atmospheric levels. In particular, Figure 4*a* shows a strong region of upper-level divergence ahead of the upper-level trough. At the 500 hPa level, a vorticity maximum is evident along the trough axis, with strong vorticity advection present in the region of cyclogenesis (Figure 4*b*). Furthermore, a robust cold front north and west of the cyclone is evident in the 850 hPa level temperature field (Figure 4*c*). The strong temperature gradient in close proximity to and west of the low-pressure center is indicative of an intensifying storm. Additionally, the tight east–west geopotential height gradient just west of the low was supportive of strong north-northwesterly boundary flow in the vicinity of the dust source region. The likelihood of strong boundary layer winds is further evident in the MSLP pattern. This pattern shows an intense midlatitude cyclone with a minimum pressure of 987 hPa. West of the low, Arctic high pressure built across Kazakhstan and into Mongolia, generating a very strong pressure gradient over the dust source region and broader Gobi Desert (Figure 4*d*).

Figure 4. (*a*) The 300 hPa height and winds, (*b*) 500 hPa height and vorticity, (*c*) 850 hPa temperature (*shaded*) and geopotential height (*black dashed contours*), and (*d*) mean sea-level pressure (MSLP; *solid black contours*) and 1,000–500 hPa thickness (*dashed color contours*). Annotations show the low center and mean surface wind direction around the low. The *blue dot* shows the approximate dust source location.

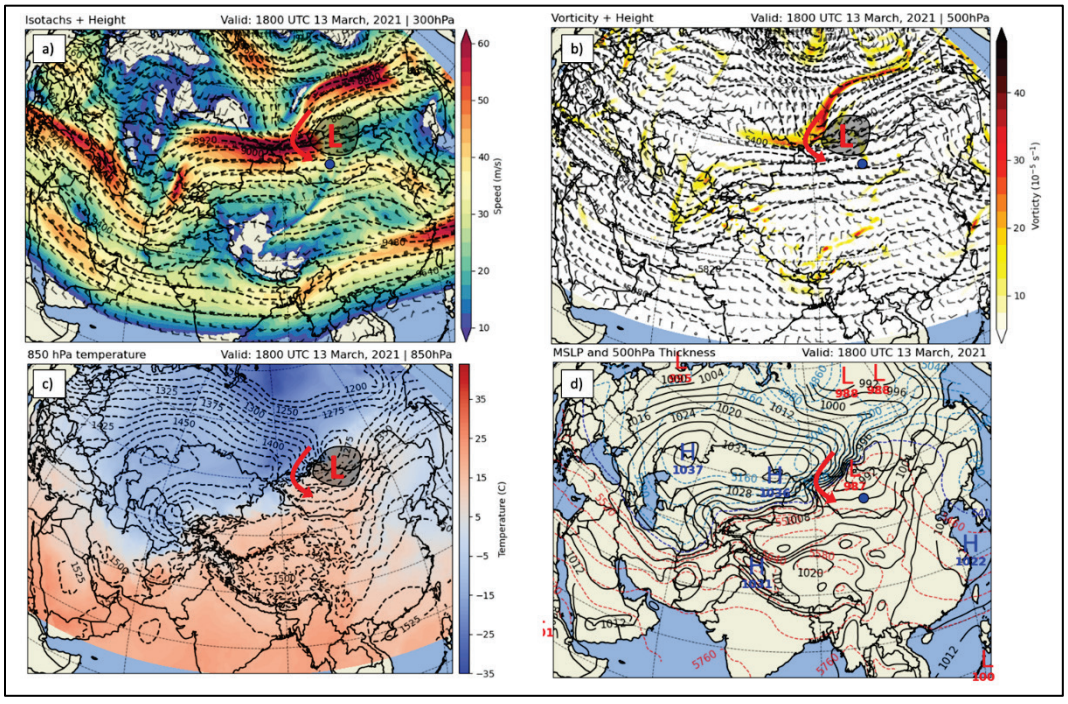

At 0600 UTC on 13 March, the surface cold front trailing behind the intensifying cyclone had just crossed over the Khangai Mountains and begun to initiate dust entrainment as the front passed over the dust source regions in the Gobi Desert (Figure 5*b*). At this time, the cyclone was still intensifying as it progressed toward Northeast China. At 1800 UTC on 14 March, the storm had reached its peak strength, with a minimum pressure below 980 hPa over Northeast China. By this time, the pressure gradient over the dust source region had markedly relaxed, and the mean wind direction shifted from northwest to a more north-northeasterly direction (Figure 5*c*). At 0600 UTC on 15 March, the storm was occluding and weakening over Northeast China. Arctic high pressure was firmly in place across Mongolia and northern China, with widespread light northerly winds. The mountains defining the northern edge of the Tibetan plateau largely blocked the southward progression of the cold air (Figure 5*d*). As strong high pressure moved in, light winds and a temperature inversion helped keep dust over the region until 20 March, when a second cold front moved south across the region and advected any remaining dust out toward eastern China and the Pacific Ocean (not shown).

Figure 5. (*a*) MSLP for 18 UTC on 13 March (same as Figure 4) and (*b*–*d*) MSLP between 06 UTC on 14 March and 06 UTC on 16 March at 12-hour intervals. The locations of the warm (*red*), cold (*blue*), and occluded (*green*) fronts are indicated on each panel. For convenience, all times are referenced to the peak of the dust emission event ($t = 0$). The *blue dot* marks the approximate location of the dust source.

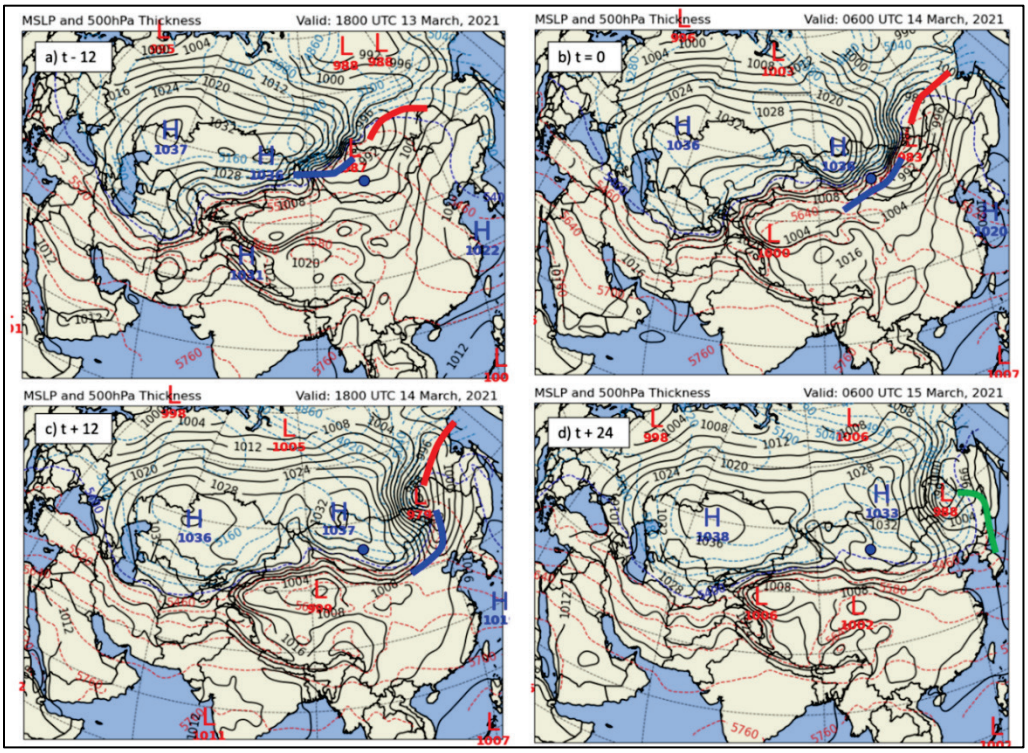

3.1.3 Dust Event Overview

Strong northwest winds that occurred over the dust source regions of the northern Gobi Desert after the passage of a cold front trailed a powerful midlatitude cyclone. Gui et al. (2022) noted that this storm was one of the strongest dust events to ever occur in the region. The poor air quality associated with the event lingered over much of northern China under quiescent conditions, trapped beneath a temperature inversion associated with an Arctic anticyclone and dammed along the northern rim of the Tibetan Plateau. To assess the evolution of this event, we used available satellite imagery from NASA Worldview and MSG-SEVIRI to identify the main dust source regions and show their southward propagation and persistence. We analyzed true-color imagery from Worldview to best identify the initial source of dust associated with the event (Figure 6).

Figure 6. NASA Worldview true-color image showing the dust plumes over Central Mongolia on 14 March 2022. The *red outline* highlights the primary region from which dust originated. The *inset* is zoomed in on the *black rectangle*. Dust plumes are visible as the *brown* and *tan linear features* aligned parallel to the mean wind, indicated by the *black arrows* in the *inset*.

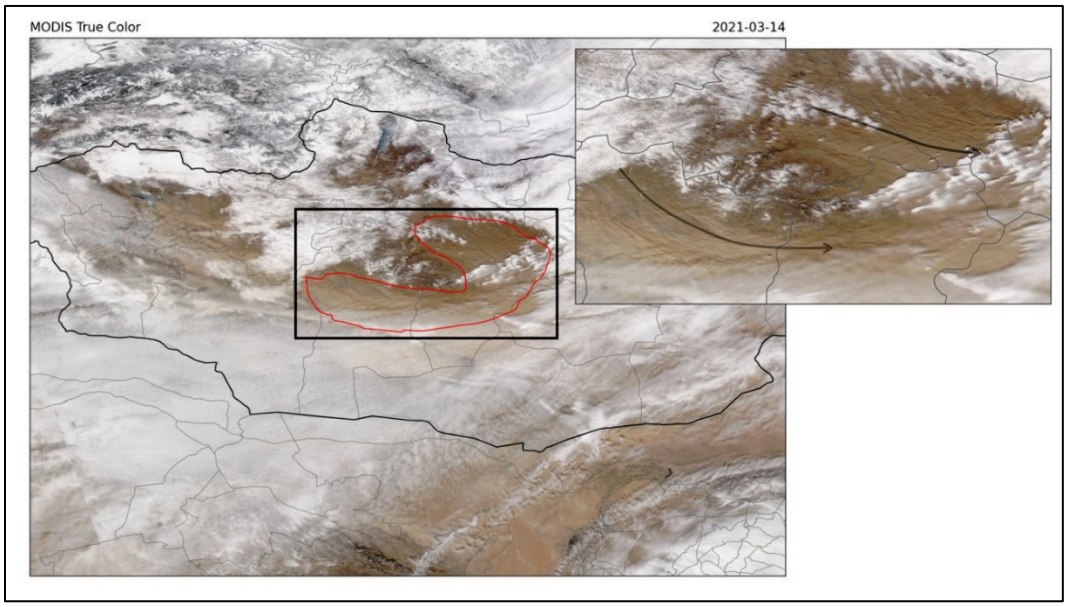

This imagery shows clear wind-aligned dust plumes occurring downstream of the snow covered Khangai Mountains in Central Mongolia. The MSG-SEVIRI false-color imagery captured during the emission event was challenging to interpret due to cloud obscuration, the diurnal cycle (which affects the color of the dust in the image), and the large off-nadir view angle that MSG-SEVIRI has of the northeastern Gobi Desert. Nevertheless, the MSG-SEVIRI imagery confirmed two key pieces of information: (1) the

contribution to the initial dust event from the Taklamakan Desert was likely small, and (2) the majority of the dust that persisted over northern China for days after the storm entered the region from dust sources north in the Gobi Desert. Figure 7 illustrates that while there was some lofted dust from the Taklamakan Desert associated with the main storm, this dust did not markedly contribute to the wider dust event that persisted over northern China. We noted a distinct lack of fuchsia coloring (i.e., pink dust) over northern China at 0100 UTC on 14 March, which is approximately six hours prior to the start of the dust emission over Central Mongolia and several hours after dust was visible over the eastern Taklamakan Desert (Figure 8).

Figure 7. Meteosat Second Generation Spinning Enhanced Visible and InfraRed Imagery (MSG-SEVIRI) false-color imagery of (*left*) 1100 UTC on 13 March 2021, approximately 18 hours prior to the passage of the cold front over the dust source region, and 14 hours later at (*right*) 0100 UTC on 14 March 2021. *Insets* for each image are indicated by the *solid-black rectangles*. Dust is identified by the *indigo-pink-fuchsia* coloring.

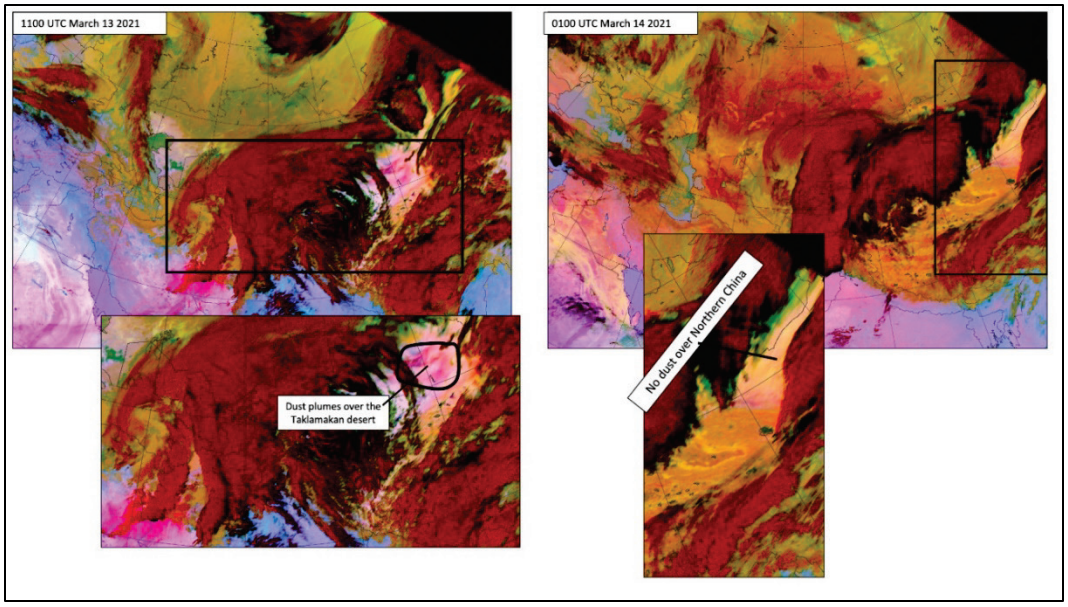

Figure 8. MSG-SEVIRI false-color imagery showing the dust plume extending along the northern rim of the Tibetan Plateau across northern China. The *rectangle* shows the inset bounds for the *insets* in Figure 10.

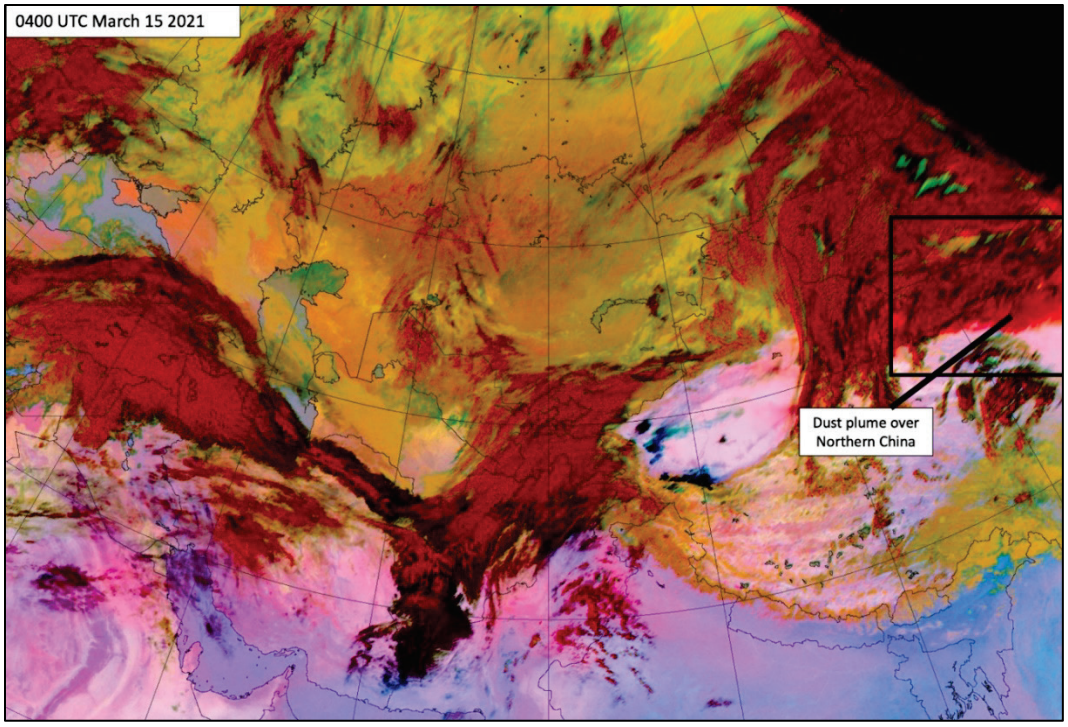

While it is difficult to discern dust at its source in the MSG-SEVIRI imagery, the plume originating from Central Mongolia can be seen progressing south through breaks in the cloud shield between 2100 UTC on 14 March and 0400 on 15 March. Figure 9 shows the dust entrenched over northern China at 0400 UTC on 15 March, approximately eight hours after the passage of the storm. The dust plume over northern China is visible as a reddish-pinkish feature that appears distinct from the deeper red clouds to the north and west. Over time, it progressed south with the building high pressure, while the main upper-level cloud shield progressed north and east following the storm. Reviewing sequential MSG-SEVIRI imagery in rapid succession (e.g., as an animated video) made these atmospheric components easier to discern. Through careful examination of MSG-SEVIRI imagery from the hours preceding the event, we were able to confirm the source of the dust feature (Figure 9).

Figure 9. (*Background*) MSG-SEVIRI imagery at 0400 UTC on 15 March (same as Figure 8). Each *inset* shows the MSG-SEVIRI imagery for the region bounded by the *solid-black rectangle* at different times prior to 0400 on 15 March. In the *insets*, the leading edge of the dust plume is indicated by the *red line*, and the general motion of the dust plume is indicated by the *blue arrows*.

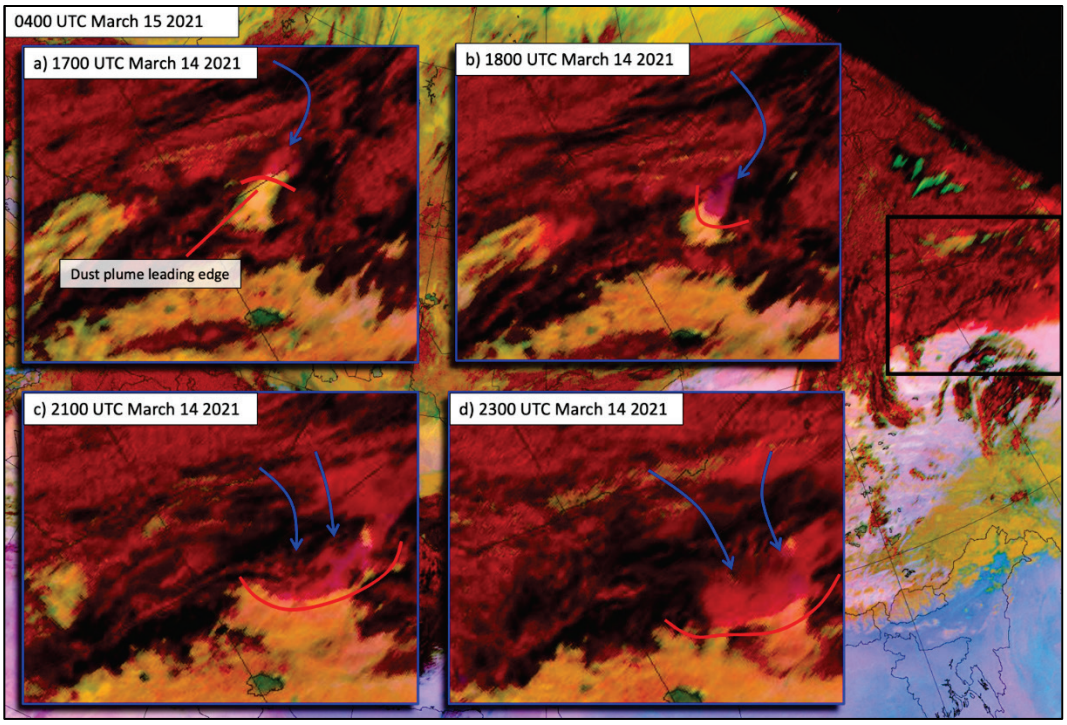

The dust plume expanded south from the dust source regions in Mongolia and spread into northern China due to the Tibetan Plateau blocking the flow to the south. At 1700 UTC on 14 March, the leading edge of the dust plume first became visible between gaps in the cloud shield (Figure 9*a*). Over the next several hours, the dust plume became more easily discerned from the clouds as it progressed south and expanded into a region with fewer clouds (Figure 9*a*–*d*). Approximately 24 hours after the plume was first discernable, at 1800 UTC on 15 March, the plume had moved out from below the cloud shield, and the dust feature was clearly visible, covering much of northern China and Mongolia (Figure 10). This widespread dust remained largely stationary for the next several days as high pressure persisted over the region (not shown).

To further support the identification of the dust source, we used the HYSPLIT dispersion model driven by GFS-FNL data. Using this configuration, we placed a point source for passive tracers at 45.07°N 102.51°E, approximately 50 km southwest of the Khangai Mountains. The model released tracer particles into the atmosphere for six hours between

0600 UTC and 1200 UTC on 14 March 2021. The north-to-south progression of the tracer particles at different times throughout the event life cycle largely mimicked the dust plume, and the tracer pattern at 0600 UTC on 15 March showed remarkable similarity to the dust plume seen in the Worldview imagery (Figure 11).

The analysis of the Worldview true-color imagery, MSG-SEVIRI false-color imagery, and the HYSPLIT model confirmed that the major dust source for this event was the northern Gobi Desert in Central and southern Mongolia and that any contributions from the more prominent dust sources in Western China and the Taklamakan Desert were likely negligible.

Figure 10. MSG-SEVIRI false-color imagery for 1900 UTC on 15 March 2021. The large dust feature is identified as the *reddish* or *fuchsia* feature extending across northern China and into Mongolia, bounded on the south by the northern edge of the Tibetan Plateau.

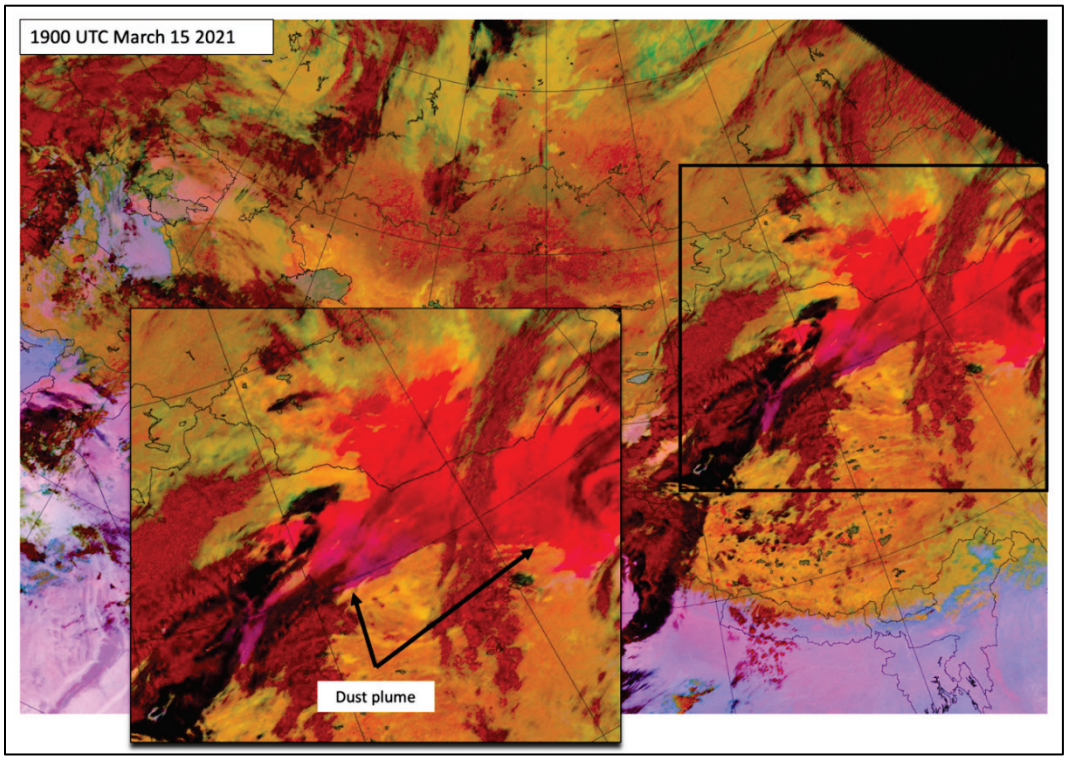

Figure 11. Worldview imagery for 15 March 2021. *Red markers* show the locations of particles released by the Hybrid Single-Particle Lagrangian Integrated Trajectory (HYSPLIT) model at a point location in Central Mongolia at different times throughout the event. The HYSPLIT model was initialized at 0600 UTC (also known as Zulu time, Z) on 14 March. The background image in this figure does not change, and the location of the HYSPLIT particles at the 24-hour time is roughly representative of the timing of the true-color image.

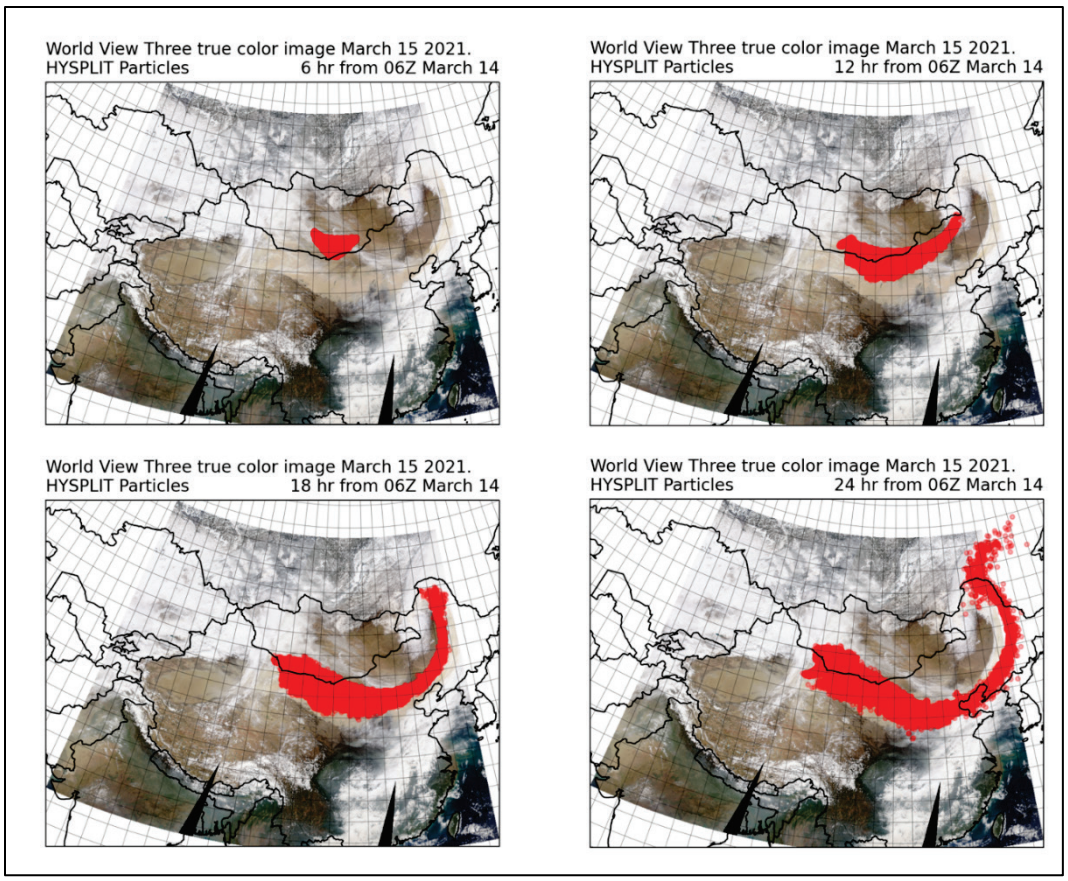

We can learn more about the dust storm by analyzing Worldview imagery and CALIPSO data in combination for the days following the passage of the storm when clear skies allowed for unobstructed views of the dust over the region. Figure 12 shows the Worldview true-color image with a CALIPSO transect overlay for 15 March 2021. The dust is clearly visible in this image as the tan feature extending along the northern rim of the Tibetan Plateau all the way to the coast before wrapping north along the cold front toward the comma-head of the occluding cyclone. The CALIPSO AOD transect overlay shows a strong increase in AOD magnitude over the main dust plume. However, patterns in the CALIPSO AOD and Worldview imagery do not align perfectly due to timing differences between their respective overpasses.

Figure 12. Worldview true-color imagery with the Cloud-Aerosol Lidar and Infrared Pathfinder Satellite Observation (CALIPSO) aerosol optical depth (AOD) on its ascending pass. Overpass occurred on 15 March 2021.

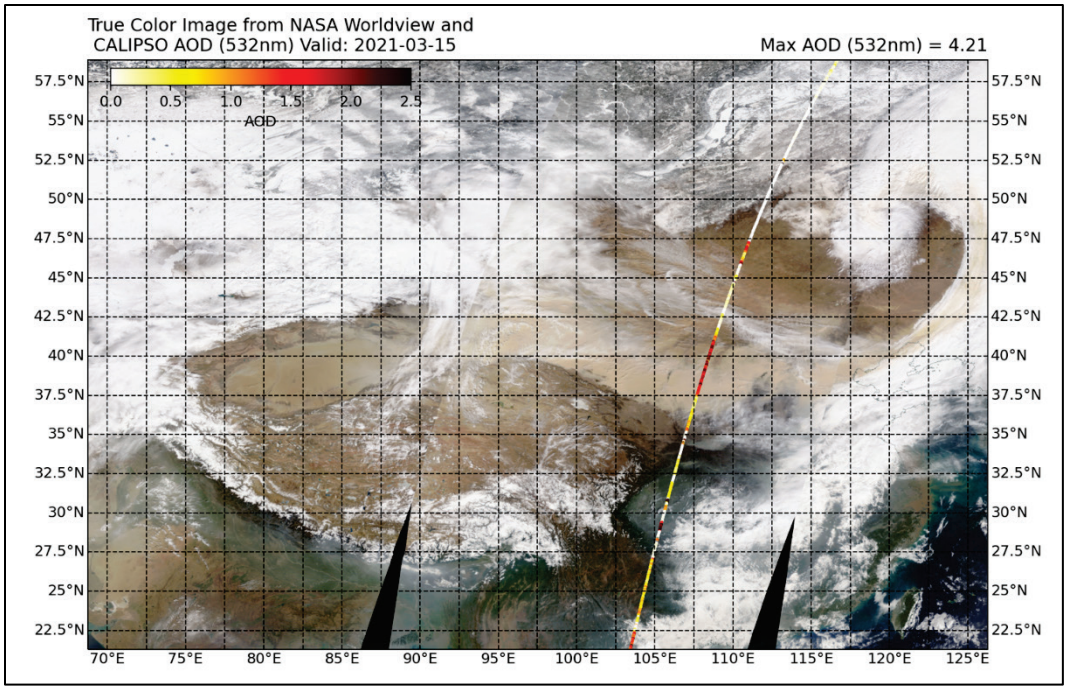

The vertical profile of the 532 nm extinction coefficient shows that the bulk of the dust is below the 700 hPa pressure level (Figure 13). However, an extension into the upper troposphere occurred north of 40°N. We speculated that this was dust that was ingested into the strong vertical motion associated with the cold-front passage and pulled into the storm. A final illustration of the event persistence shows Worldview true-color imagery for 15, 16, and 18 March (Figure 14). Figure 14 clearly shows the effect of the elevated terrain in holding the dust in place near the surface for a prolonged period following the passage of the storm after 14 March.

Figure 13. (*Top*) CALIPSO extinction coefficient vertical cross section from south to north (*color shaded*). The *solid-blue shading* indicates clouds. The *outlined gray surface* shows the approximate ground surface. (*Bottom*) Column-integrated AOD for the yellow-visible (532 nm) and near-infrared (NIR; 1,064 nm). The main dust plume is between the 35°N and 42°N latitude bounds.

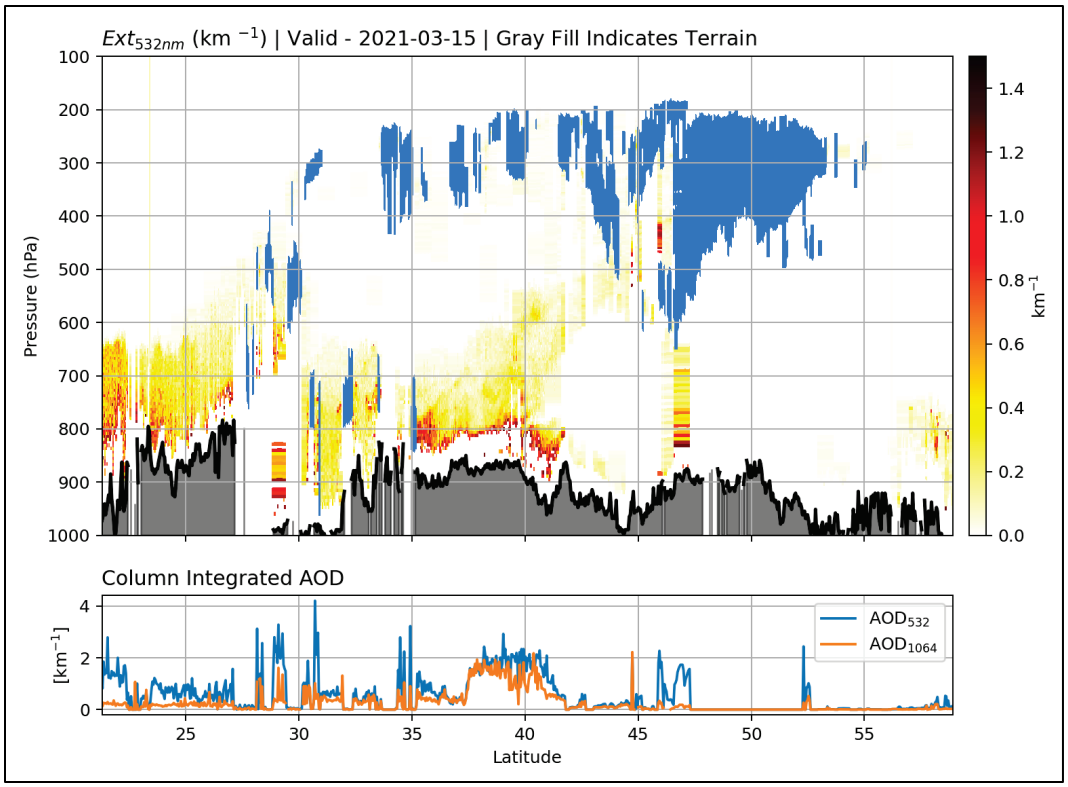

Figure 14. Worldview true-color imagery for (*top* to *bottom*) 15 to 18 March 2021.

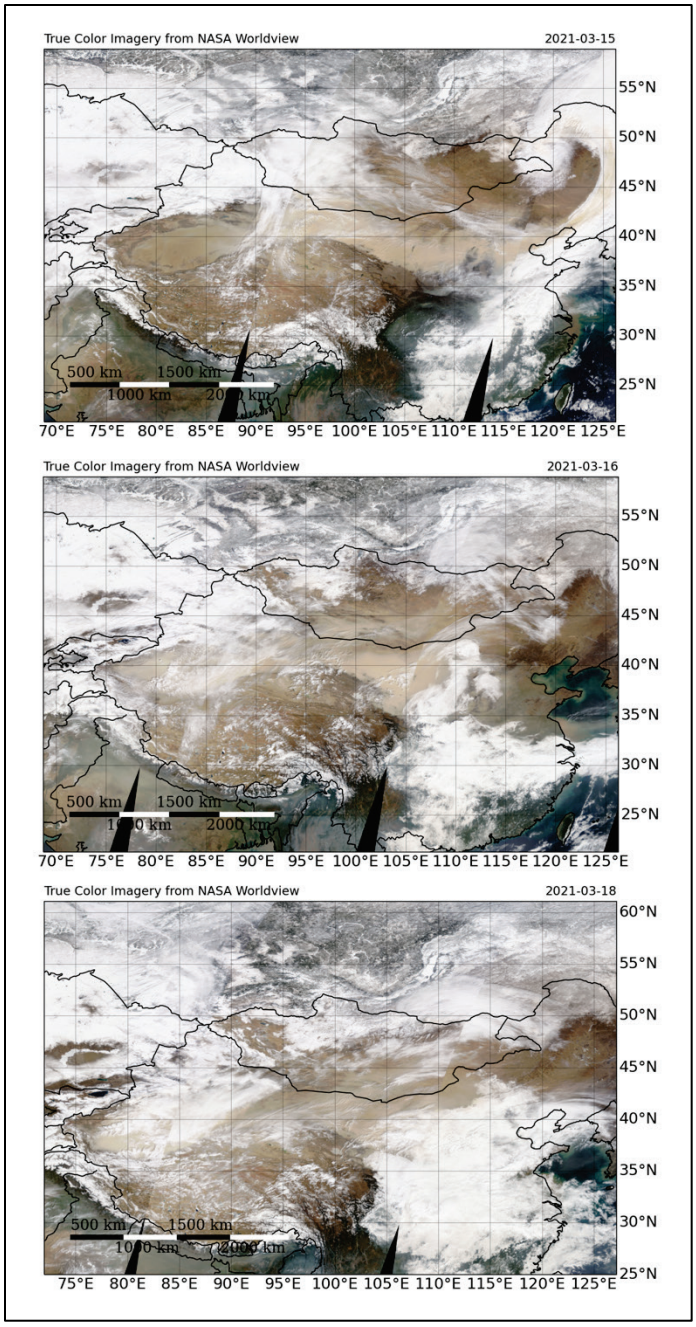

In summary, we concluded that this dust event was a strong, long-lived event that was only meteorologically active during its initial phase. The main dust source for this event was the northeastern Gobi Desert south of the Khangai Mountains in Central Mongolia. A successful simulation of this event would require the accurate simulation of the baroclinic wave that formed the midlatitude cyclone. Further, it would require accurate representation of any possible effects that the Khangai Mountains had on

the boundary layer as the front crossed the mountains into the adjacent dust source regions. After the initial dust emission phase, an accurate simulation of the persistent dust effects across northern China would require a proper simulation of the cold air damming along the Tibetan Plateau and an accurate representation of the dust deposition process. Additionally, the simulation should incorporate the antecedent diminished snow cover and anomalously dry soils present across the dust source region. Accordingly, the model's land surface initialization is important for this event.

3.2 Dunhuang, China, 24–25 July 2021

3.2.1 Event Overview

A severe convective dust event originated along the outflow boundary of a *mesoscale convective system* (MCS) on the afternoon of 25 July 2021 between 1400 and 1500 local time (LT; 0700–0800 UTC). The dust storm created hazardous air quality conditions for the city of Dunhuang in northwest China. Several news organizations reported visibilities dropping below 6 m at times and shared dramatic videos of a towering wall of dust engulfing the city. Because the key driver of the storm was a convective system that occurred in a data-sparse region, subjective interpretation of the MSG-SEVIRI satellite data is arguably the best tool for characterizing the event's evolution. We further supplemented the satellite imagery assessment with ERA5 reanalysis to gain insight into the large-scale environment that supported the development and life cycle of the MCS. The ERA5 product does not provide any information regarding the MCS itself due the mesoscale nature of the MCS phenomenon.

3.2.2 Synoptic Overview

The main synoptic features associated with this event included a large upper-level blocking high pressure centered over interior Russia, a weak upper-level trough with its axis centered over Northwestern China, and an amplified upper-level shortwave trough embedded within the broader flow. Approximately 24 hours prior to the event, the center of a broad upper-level ridge of high pressure propagated over interior Russia with a trough of low pressure located upstream of Dunhuang near where the borders of Russia, Kazakhstan, China, and Mongolia intersect (Figure 15*a*). South of the trough, the Tibetan High (a common summer time meteoro-

logical feature characterized by persistent high pressure in the upper troposphere over the Tibetan Plateau) remained firmly in place, facilitating broad anticyclonic upper-level flow over much of China.

Figure 15. The 300 hPa isotachs from the ERA5 reanalysis showing the upper-level synoptic pattern at approximately (*a*) 24, (*b*) 12, and (*c*) 6 hours prior to the event and (*d*) 6 hours after the event. Specific times are indicated on the figure by time minus duration (i.e., *t* – number). The location of Dunhuang is marked with a *blue marker*. The approximate axis of the upper-level trough that organized the convection is marked by the *red dashed line*.

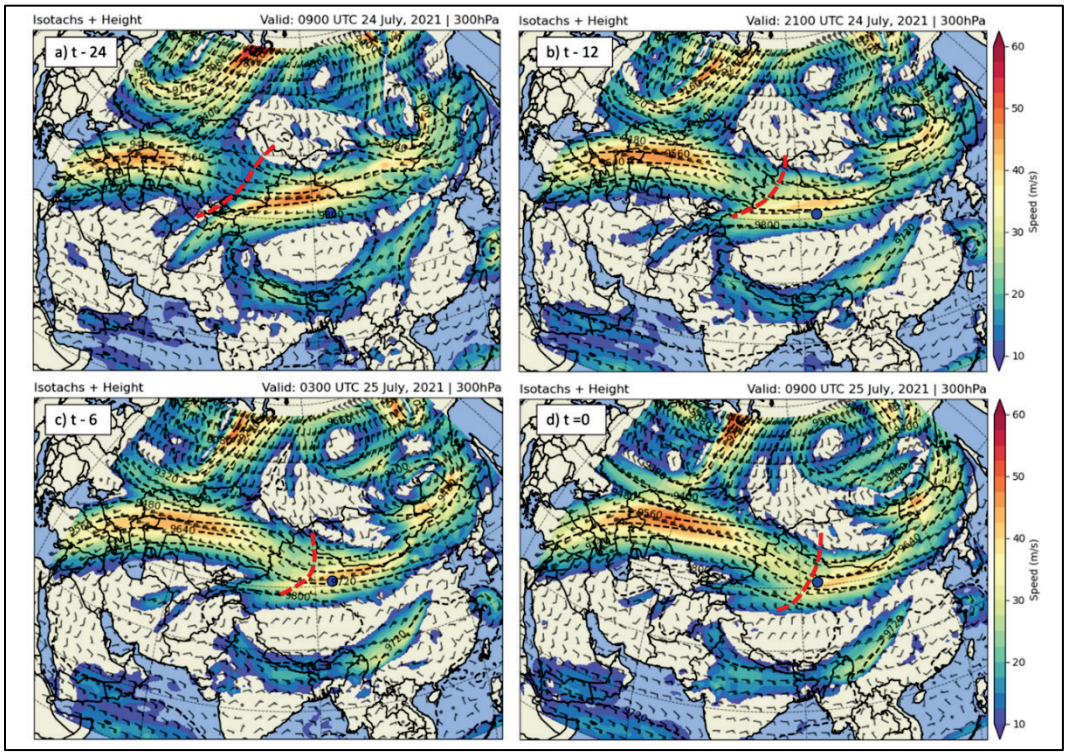

The tightening geopotential height gradient between the low and the northern extent of the Tibetan High enhanced the subtropical jet stream. As the trough over China progressed east, the subtropical jet stream gradually moved south of Northwestern China, and the jet core shifted toward Dunhuang in the hours leading up to the event (Figure 15*b*, *c*). At the time of the event, Dunhuang was almost directly beneath the upper-level trough axis and near the equatorial jet entrance region. This upper-level pattern favored synoptic-scale upward vertical motion over Dunhuang, which facilitated convective growth and organization. After the event, the shortwave moved east of the area, allowing for northwest upper-level flow to persist over the region (Figure 15*d*).

To assess the convective potential of the environment, we analyzed a skew-T, log-p diagram that showed the vertical profile of the atmosphere from

the ERA5 reanalysis (Figure 16). In particular, we assessed atmospheric convective instability using a common quantitative metric called Convective Available Potential Energy (CAPE). CAPE essentially quantifies how much buoyancy an air parcel lifted from near the surface has as it rises through the atmospheric column. High values of CAPE (i.e., CAPE > 1,000 J kg^{-1}) generally indicate deep *convection* and strong thunderstorms. We also reviewed the skew-T log-p diagram to discern the degree of windshear, which helps organize convection.

This analysis showed that the thermodynamic environment in the vicinity of Dunhuang near the time of the event was very dry in the lower troposphere, with a nearly dry-adiabatic temperature profile persisting to approximately 600 hPa (Figure 16). The dry boundary layer resulted in only modest instability, with the most unstable CAPE (i.e., MUCAPE < 100 J kg^{-1}) and an equilibrium level (EL) of approximately 400 hPa. Upstream of Dunhuang, where the convection initiated, the thermodynamic profile was similar, with a dry, deep boundary layer. However, this upstream location also had a slightly more unstable environment (i.e., MUCAPE of approximately 400 J kg^{-1}), making conditions more conducive to convective initiation (not shown). In both environments, a stable layer at approximately 450 hPa, characterized by a nearly isothermal temperature profile, prevented deeper convective growth. Accordingly, the convection that led to the dust storm was relatively shallow compared to the deeper convection over the Tibetan Plateau. However, while the convection was relatively modest, the dry and deep boundary layer highly supported evaporative cooling and the development of negatively buoyant downdrafts beneath the convective system. Further, strong winds aloft, associated with the jet stream, resulted in nearly 70 kn of bulk shear between the 850 and 500 hPa levels. This shear organized the relatively modest convection and likely facilitated strong winds near the surface through downward convective mixing. So while the area had limited instability, the windshear and downdraft potential were supportive of MCS organization and strong surface winds.

Figure 16. Skew-T log-P diagram for Dunhuang from the ERA5 reanalysis. Common convective and severe weather indices are indicated on the top right. The red line indicates temperature, and the green line indicates dew point. The black line shows the temperature of an air parcel lifted from the surface as it rises until it forms a cloud at the lifted condensation level (LCL), becomes positively buoyant at the level of free convection (LFC), and then becomes negatively buoyant at the equilibrium level (EL). Wind barbs with speeds in terms of knots are shown on the right-hand side of the figure. The *inset* plot on the bottom right shows a hodograph trace of the wind speed and direction with height. Additional storm-related indices, storm relative helicity (SRH) and convective inhibition (CIN), are provided for extra context.

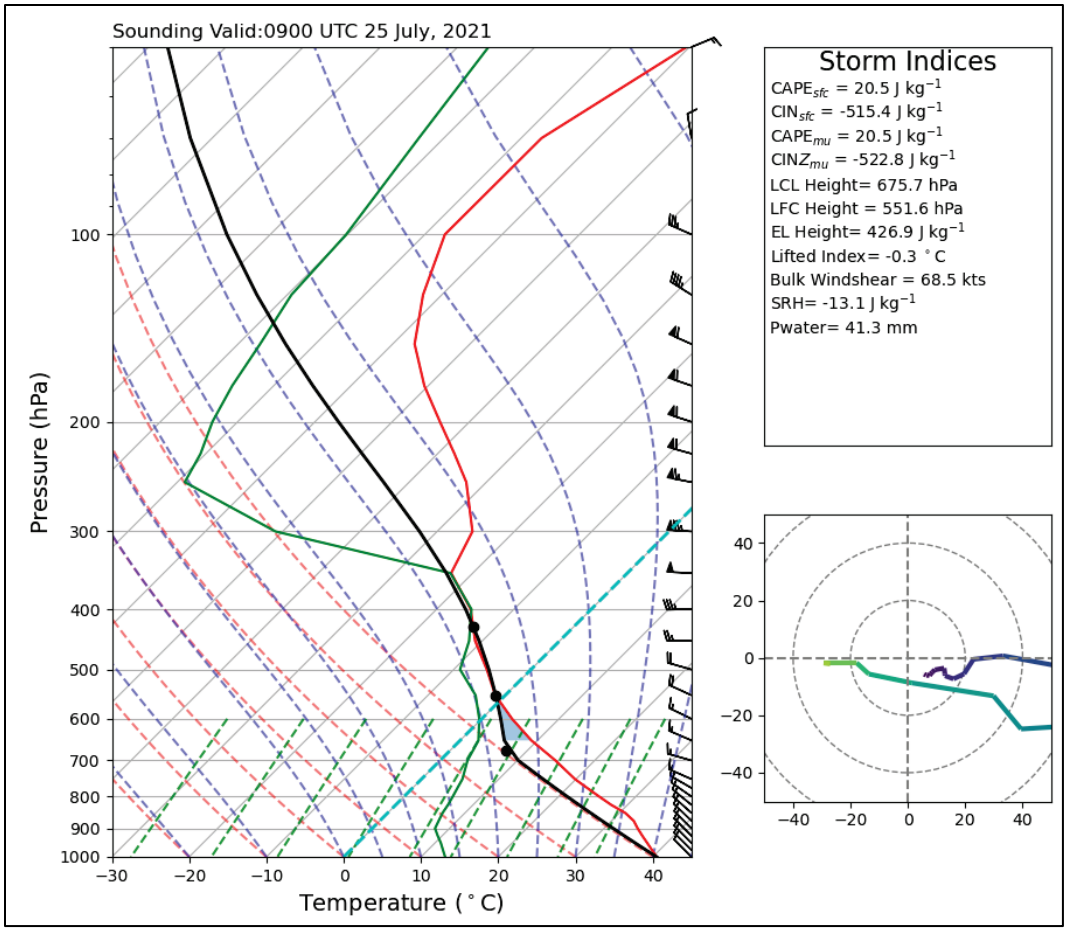

Subjective analysis of satellite imagery from MSG-SEVIRI and MODIS served as the best means to assess the overall evolution of the convective activity associated with the event. At 0000 UTC on 25 July 2021, disorganized cloudiness was visible along and ahead of the upper-level trough axis (Figure 17*a*). As the day progressed, broad anticyclonic flow around the Tibetan High, aided by the southeastward progression of the upper-level trough, helped initiate and organize deep convection over the Tibetan Plateau and the Himalaya mountains (seen as the deeper reds in Figure 17*b*–*d*, well south of the dust event). To the northwest of Dunhuang, persistent cloudiness along the western Taklamakan Desert beneath the core of the jet served as an early indicator of where convection would develop

(Figure 17*a*). This cloudiness gradually progressed east with the upper-level trough and initiated new convection north and west of Dunhuang along a northeast trajectory (Figure 17*b*). This convection grew upscale (i.e., the convection changed its morphology) and organized, facilitated by upper-level divergence and large-scale upward vertical motion ahead of the upper-level shortwave trough. As the convective system approached Dunhuang, it organized into a quasi-linear MCS and pivoted to a south-easterly trajectory as new cells developed along the downstream outflow boundary (Figure 17*c*–*d*).

Figure 17. Annotated MSG-SEVIRI false-color satellite images at different times throughout the event. Dunhuang is marked with a *red marker*. The *dashed black line* shows the approximate location of the upper-level trough axis. *Arrows* indicate the approximate storm motion of the convective elements composing the mesoscale convective system (MCS).

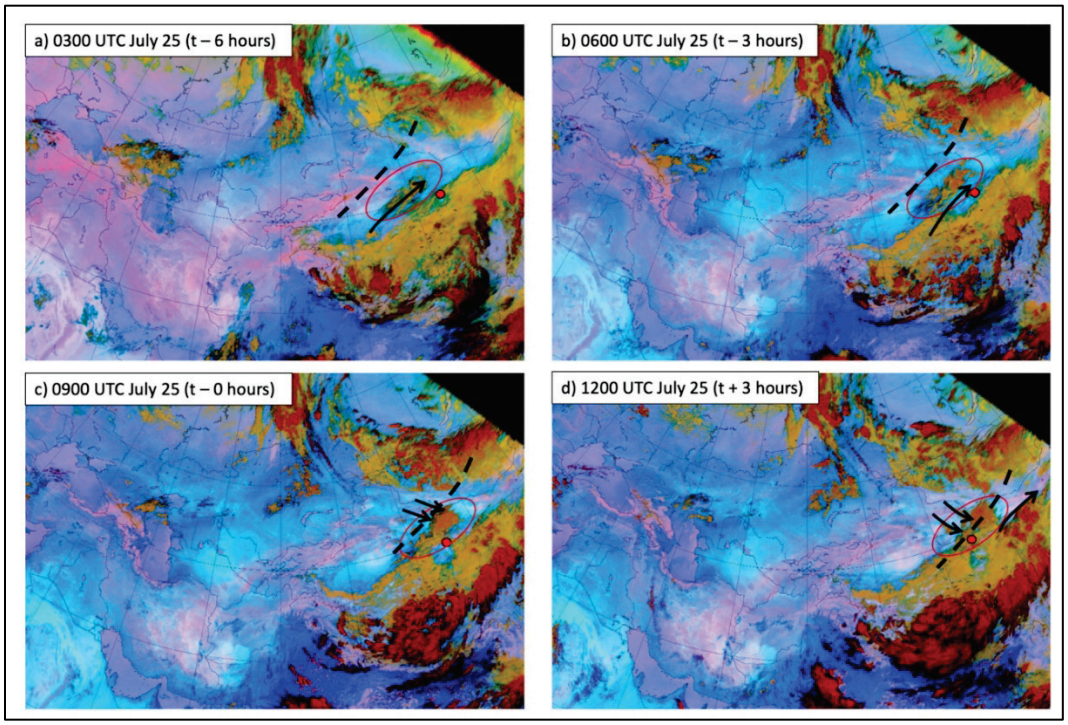

Worldview true-color imagery provided qualitative information on the storm morphology at two different times during the MCS life cycle (Figure 18). The MODIS Aqua and Terra satellites that collected these images passed over the region at different times. Both of these snapshots occurred prior to the dust event. The Terra overpass (the earlier of the two) shows the MCS in its early stage, when it was composed mostly of new discrete convection, with convective initiation favoring areas over elevated terrain features due to the influence of orographic lift (Figure 18*a*). The Aqua overpass, which shows the MCS just prior to the dust event, displays a

more mature MCS with enhanced cloudiness immediately along the system's eastern outflow boundary, indicating a robust downdraft (Figure 18*b*).

Figure 18. (*Top*) MODIS Terra true-color image from NASA Worldview on 25 July 2021 showing the initiation of convection. (*Bottom*) MODIS Aqua true-color image from NASA Worldview on 25 July, valid approximately three hours after the Terra overpass, showing a mature quasi-linear MCS approaching Dunhuang. Dunhuang is marked by the *red star* in both images. Approximate timing for each satellite overpass is indicated in local time (LT).

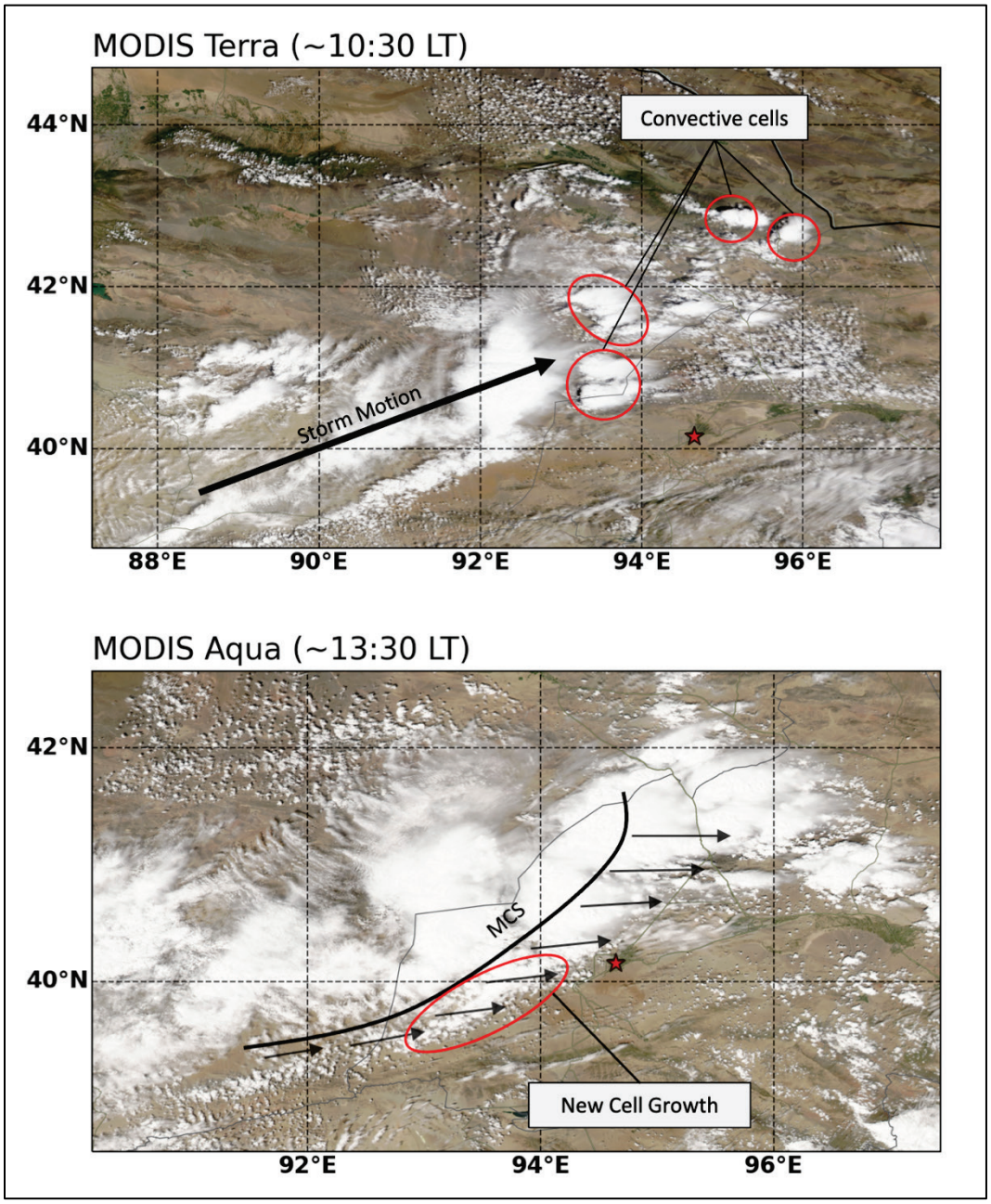

In summary, this dust event resulted from outflow along an organized MCS. From a numerical modeling perspective, a properly configured mesoscale weather model should be able to reproduce the location and timing of the upper-level, large-scale trough and jet stream that facilitated the growth and organization of convective activity and the deep, dry boundary layer that supported the robust downdrafts. Additionally, a successful model simulation should generate convection in roughly the right area. Fortunately, upper-level synoptic features largely anchored convective activity associated with this event to specific locations, and the convection organized at resolvable scales for most convective-permitting simulations. However, if the weather model's land surface functions or atmospheric surface layer schemes are prone to forming overly dry environmental conditions, the resultant simulations may inadvertently limit or suppress convective initiation due to issues with instability formation or dry boundary layer conditions.

3.2.3 Dust Event Overview

Assessing the evolution of the dust transport associated with this event is generally straightforward. To the best of the authors' knowledge, there are no open access, continuous monitoring, in situ visibility or dust measurement stations that recorded adverse conditions associated with the storm. Moreover, while the MODIS retrievals were helpful for assessing the structure of the convection, the sensors did not collect imagery for the area of interest (AOI) during the actual dust event. Finally, the nearest CALIPSO overpass occurred between 2000 and 2100 UTC, approximately eight hours after the event had ceased. As a result, we limited our assessment of the dust conditions to MSG-SEVIRI imagery interpretation and commentary from available news reports.

Dust became visible in the MSG-SEVIRI false-color imagery around 0900 UTC along the leading edge of the MCS (Figure 19). By 1000 UTC, a well-defined region of dust appeared ahead of the MCS over the vicinity of Dunhuang (Figure 19*c*). At 1100 UTC, cloudiness obscured most of the dust plume in the satellite imagery, but we can infer the presence of dust east of Dunhuang by the faint traces of bright pink along the edges of cloud-covered areas (Figure 19*d*). From 1200 UTC onward, the dust plume remained obscured in the satellite imagery for the rest of the event lifecycle (Figure 19*e*).

Figure 19. MSG-SEVIRI false-color imagery showing the dust plume (indicated by *pink* or *fuchsia* shading) at (*a*) 1000 UTC on 25 July 2021, large domain, and (*b*–*e*) 0900–1200 UTC on 25 July, zoomed into the region bounded by the *dashed box* in image (a). Annotations are provided to highlight the location of the dust plume in the MSG-SEVIRI imagery. Approximate location of Dunhuang is indicated by the *red marker*.

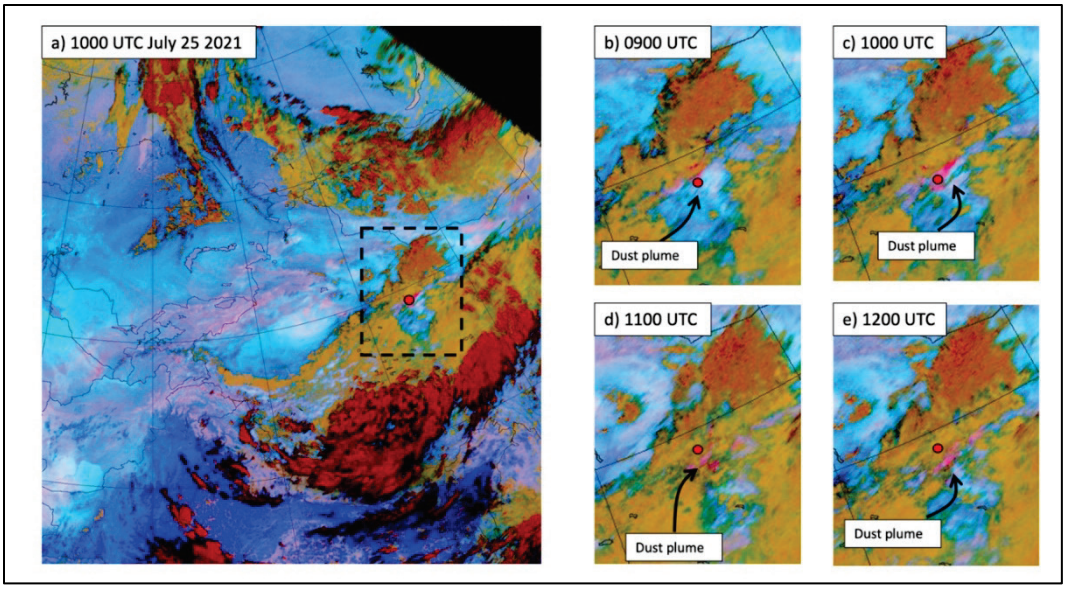

At its peak, the dust plume stretched approximately 100 km from southwest to northeast along the outflow boundary of the MCS. According to news reports from the British Broadcasting Company (BBC), the storm generated a wall of dust extending up to 100 m in height that severely reduced visibility in Dunhuang (BBC News 2021). Overall, hazardous air quality conditions created by the storm affected an approximately 40,000 km² region for approximately three hours. Interestingly, a second convectively driven dust event occurred the following day, on 26 July 2021, southeast of Dunhuang (not shown). This second event was more coherent in the satellite imagery and affected a larger area. However, because the event did not affect any heavily populated regions, this second event went largely unnoticed by the media. Nonetheless, this follow-on dust event could be an additional case study opportunity for evaluating convective-resolving dust transport and air quality models.

3.3 Kazakhstan and Uzbekistan, 3–6 November 2021

3.3.1 Event Summary

Between 3 and 6 November 2021, a strong dust event resulted from strong low-level winds generated by interactions of an anticyclonic circulation moving in from the northwest with the complex topography of the Tian

Shan Mountain Range in southeastern Uzbekistan. Strong winds along the southern edge of the anticyclone occurred near the border of southern Kazakhstan on 4 November, eroding the surface soil and transporting dust aerosols southward into Uzbekistan. We suspect that localized, strong, low-level winds associated with the exit regions of narrow gaps or low areas in the mountainous terrain (i.e., gap winds) upwind of the dust sources may have increased the dust emissions. The Uzbekistan Meteorological Service reported strong surface winds reaching 20–25 m s^{-1} in the Jizzax, Navoi, and Bukhara regions of Kazakhstan (Figure 20; Center of the Hydrometeorological Service of the Republic of Uzbekistan, n.d.). News agencies in the area reported that the dust plume caused a maximum reduction in visibility to below 200 m in the city of Tashkent at 1821 LT on 4 November. This event was short-lived, with a dense dust plume and a relatively small spatial extent compared to the other synoptically driven events discussed in this report. Accounts from several news sources also indicated that this dust event was the first of its kind since record keeping began 150 years ago (e.g., Eurasianet 2021; Watchers 2021). The most affected areas were near Tashkent and areas to the southwest near the Syrdarya Region, and the primary dust source region for this event was the eastern portion of the Kyzylkum ("Red Sand") Desert in Kazakhstan and Uzbekistan.

Figure 20. Zoomed-in view of the general area of interest (AOI) for the 3–6 November 2021 dust event. *Inset* shows the general synoptic set up over a larger region, with the *zoomed-in* box indicated. The *red box* shows the general region where dust emission was widespread. (Map image is the intellectual property of Esri and is used herein under license. Copyright 2020 Esri and its licensors. All rights reserved.)

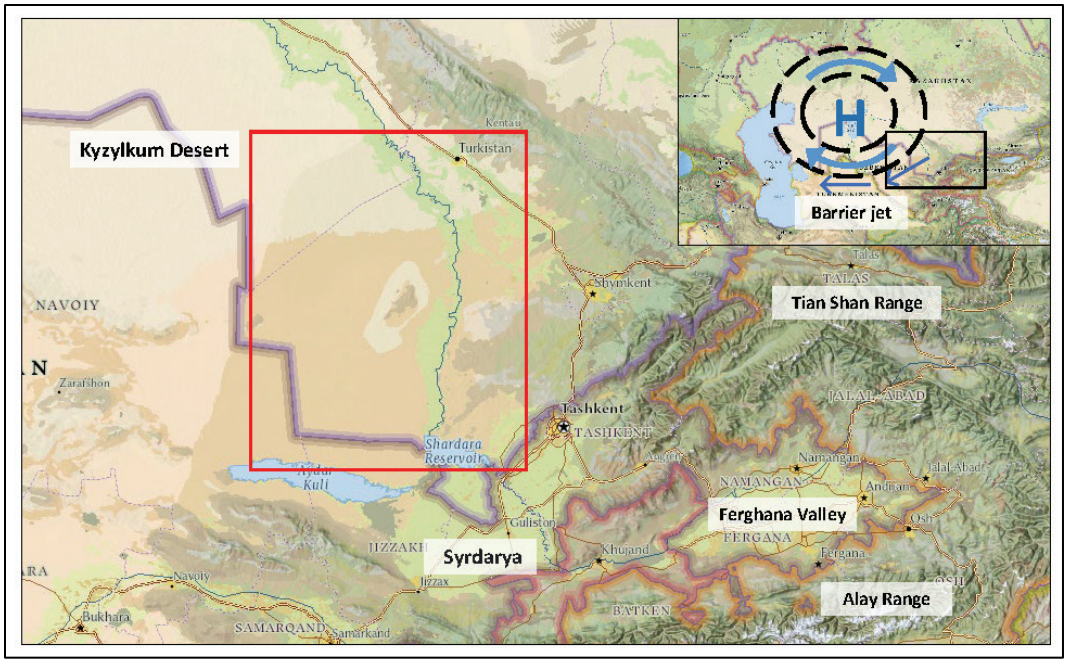

3.3.2 Synoptic Overview

A highly amplified upper-level trough or ridge pattern characterized the synoptic setup for this event as it moved into the region from the northwest. At 0000 UTC on 3 November 2021, the base of a positively tilted upper-level trough centered over northeast Kazakhstan, with the trough axis extending through the center of the country in a northeast to southwest orientation (Figure 21*a*). The 300 hPa trough included jet streaks west of the trough axis, with winds reaching speeds of up to 65 m s^{-1} over northern Kazakhstan. On 4 November, the trough extended further south and westward as an anticyclonic wave-break pattern moved over portions of western Kazakhstan and Uzbekistan (Figure 21*b*). Upper-level winds turned from north to northeasterly across central Kazakhstan along the left entrance region of the trough. Strong upper-level winds (>60 m s^{-1}) associated with the 300 hPa jet began wrapping around the southeastern quadrant of the anticyclone over the 3–5 November time frame (Figure 21*c*). As the upper-level anticyclone entered the region on 4 November, subsidence and cold-air advection created an environment favorable to gap winds and *barrier jet* dynamics on the greater Tian Shan Mountain Range. In particular, cold air damming along the north of the Tian Shan Mountain Range and a strong north–south pressure gradient favored enhanced winds west of the Tian Shan Mountains along the Kazakhstan and Uzbekistan border.

On 3 November, the 0000 UTC 850 hPa ERA5 analysis displayed strong cold air advection over northern and central Kazakhstan as the ridge over western Russia moved southeastward (Figure 22*a*). The cold air mass was moving southward toward the Tian Shan Mountain Range to the southeast. As the cold air mass began to dam behind the mountain range, a strong southeasterly pressure-gradient flow developed parallel to the mountain range (Figure 22*b*). The 0000 UTC surface wind analysis for 3 November showed that winds were the strongest across central Kazakhstan, reaching speeds of approximately 13 m s^{-1}.

Figure 21. The 300 hPa heights and winds illustrating the precursor upper-level dynamics ahead of the event.

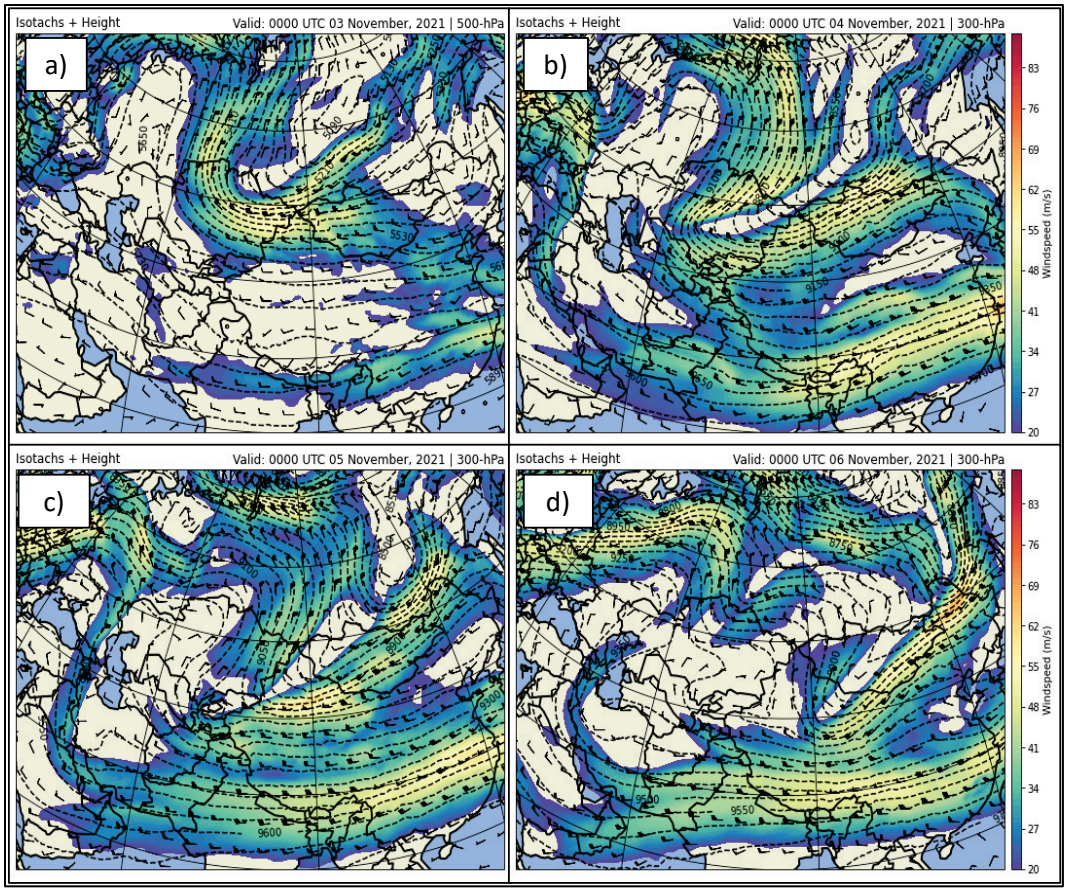

Figure 22. (*a*) The 850 hPa temperature and heights and (*b*) MSLP and surface wind speed for 00 UTC on 3 November 2021.

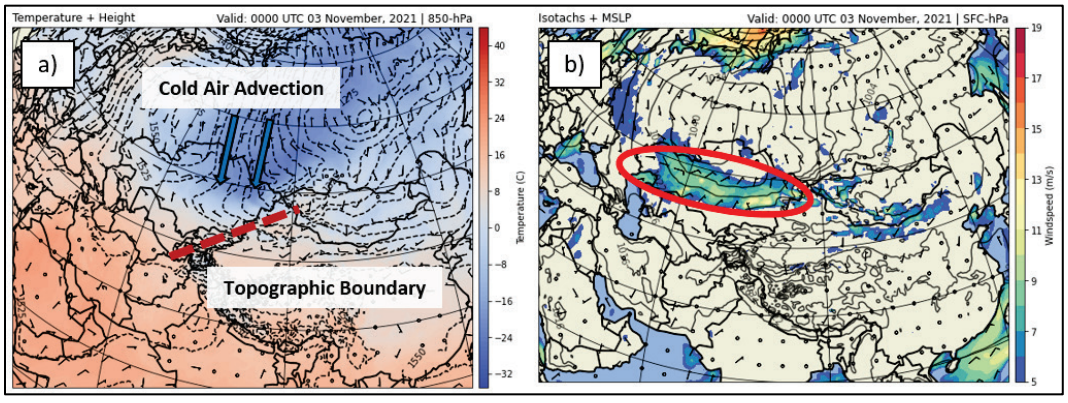

Twenty-four hours later, on 4 November at 0000 UTC, the 850 hPa ERA5 analysis showed the cold front moving into Uzbekistan as the center of the polar anticyclone propagated southward (Figure 23*a*). As cold air continued to advect into the region, temperatures decreased along the northern side of the Tian Shan Mountains. We hypothesized that gap-wind effects

likely enhanced the area of strong surface winds downstream of the mountains and south of the anticyclone (Figure 23*b*), with wind speeds >15 m s^{-1} and the strongest winds shifting southwestward to areas along the border of Kazakhstan and Uzbekistan. It was around this time that the winds began to entrain dust into the atmosphere.

Figure 23. (*a*) The 850 hPa temperature and heights and (*b*) MSLP and surface wind speed for 00 UTC on 4 November 2021.

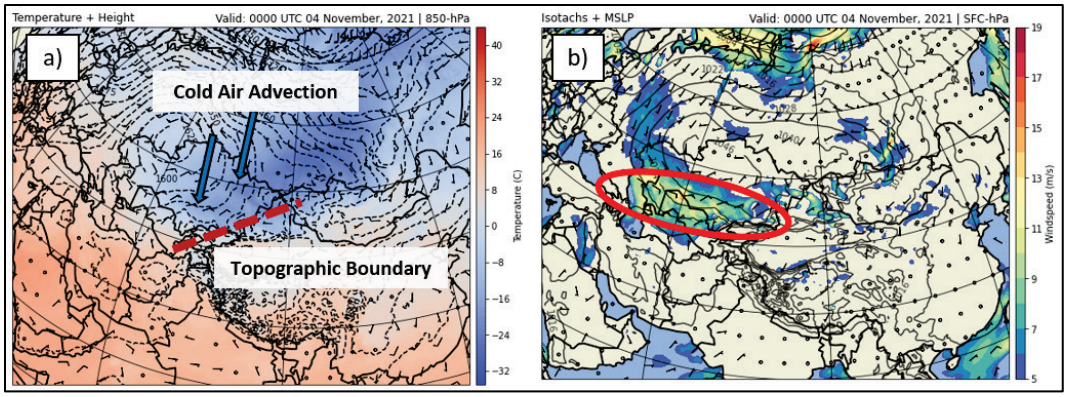

The Zhambyl, Kazakhstan (approximately 250 km northeast of Tashkent) atmospheric sounding analyses for 4 and 5 November at 1200 UTC show a notable, approximately 870 hPa temperature inversion that likely contributed to the strong gap flow along the northwestern valley of the Tian Shan Mountains (Figures 24 and 25). Gap wind processes tend to amplify wind speeds under strong temperature inversions that trap cold air near the land surface due to the strong surface pressure gradient that forms between the area under the inversion upstream of the mountains and the downstream area. This particular atmospheric environment likely forced air to rapidly flow through the small gaps or narrow channels in the mountains rather than to ascend over them.

Figure 24. Skew-T log-P diagram generated from *radiosonde* data collected from Zhambyl, Kazakhstan at 12 UTC on 4 November 2021. The *red line* indicates temperature, and the *green line* indicates dew point. The *black line* shows the temperature of an air parcel lifted from the surface as it rises throughout the atmospheric column. Wind bars are shown on the *right-hand side* of the figure.

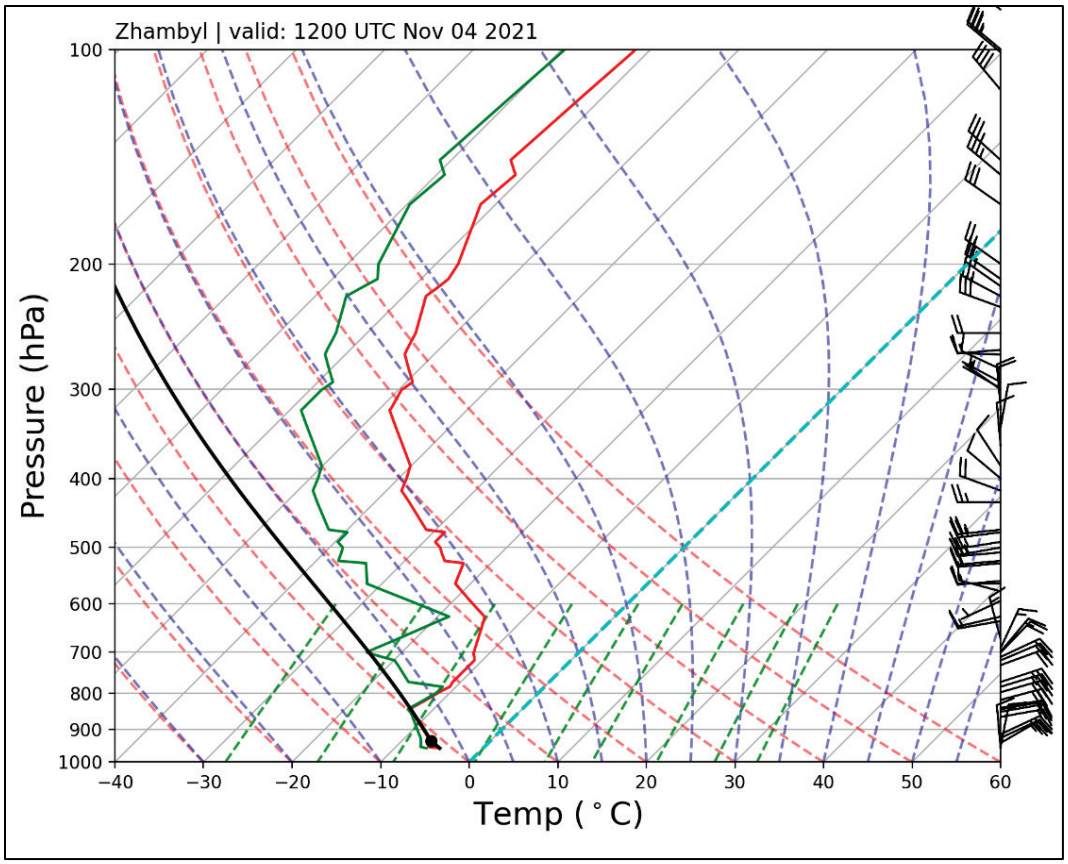

Figure 25. Skew-T log-P diagram generated from radiosonde data collected from Zhambyl, Kazakhstan at 12 UTC on 5 November 2021. The *red line* indicates temperature, and the *green line* indicates dew point. The *black line* shows the temperature of an air parcel lifted from the surface as it rises throughout the atmospheric column. Wind bars are shown on the *right-hand side* of the figure.

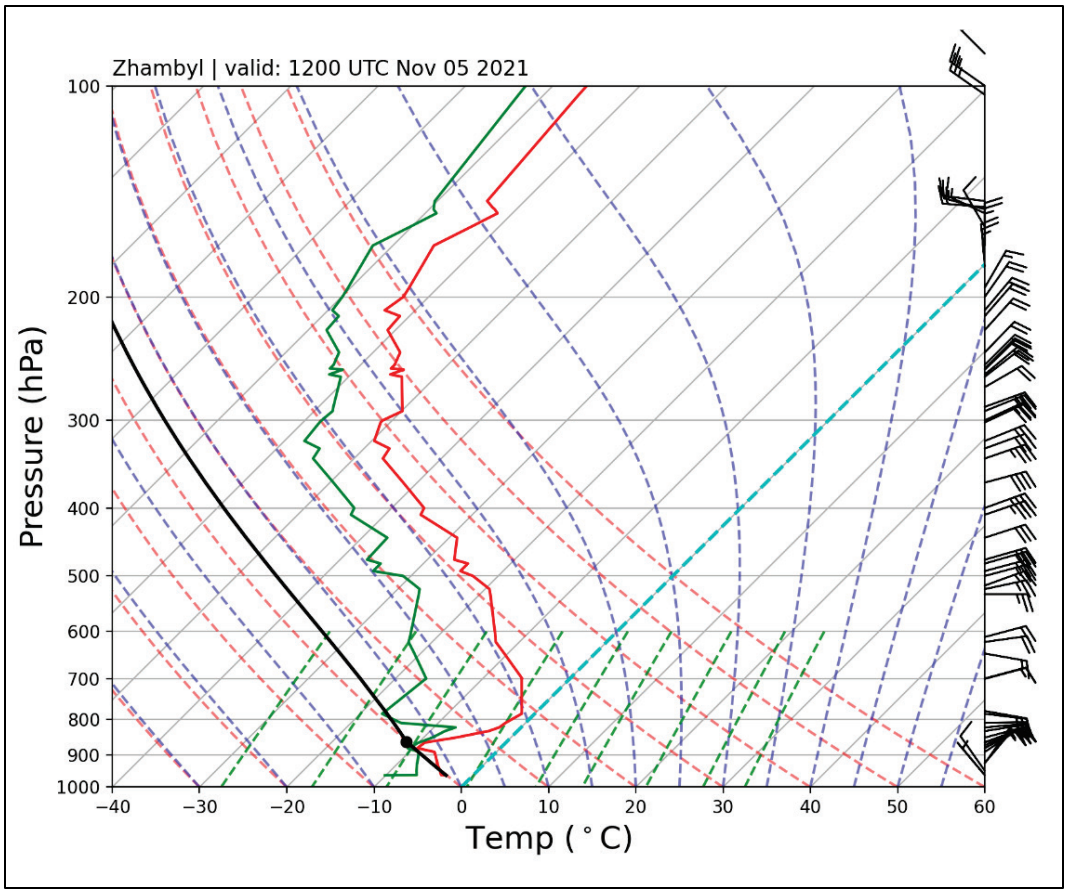

The strong surface winds exited the region to the southwest as the center of the high-pressure circulation moved directly over the area on 5 November.

In summary, this event resulted from an anticyclonic wave-break pattern that influenced an area of enhanced surface winds northwest of the Tian Shan Mountain Range, along the Kazakhstan and Uzbekistan border. For a numerical weather model to successfully represent the event, the simulation should accurately reproduce the timing and placement of the anticyclonic wave-break pattern that moved over portions of western Kazakhstan and Uzbekistan. The model simulation would also need to accurately reproduce the subsidence and cold-air advection that resulted in cold air damming along and north of the Tian Shan Mountain Range. This pattern, combined with the topography of the area, resulted in a strong

north–south pressure gradient that created an environment favorable for a barrier jet and gap wind event.

3.3.3 Dust Event Overview

Because a convection-free, high-pressure circulation drove the mechanisms of this event, subjective interpretation of the MSG-SEVIRI false-color and MODIS true-color satellite imagery provided a relatively clear understanding of the dust event evolution. Dust was first visible in the MSG-SEVIRI false-color imagery around 0400 UTC, just north of the border of Uzbekistan. By 0600 UTC, a well-defined dust plume was apparent over the same area with a north-to-south orientation across the border of Kazakhstan and Uzbekistan (Figure 26). The dust plume appeared to intensify and advect southwestward in the 1200–1800 UTC imagery. By 0000 UTC on 5 November, the dust plume began to dissipate as strong low-level winds exited the area.

Figure 26. MSG-SEVIRI false-color imagery showing the dust plume (indicated by *pink* and *fuchsia* shading). (*Left*) Large domain at 0400 UTC on 4 November. (*Center* and *right*) Imagery from 4 November at 0600 to 5 November at 0000 UTC, zoomed into the region bounded by the *dashed box* in the image on the *left*. Annotations are provided to highlight the location of the dust plume in the MSG-SEVIRI imagery.

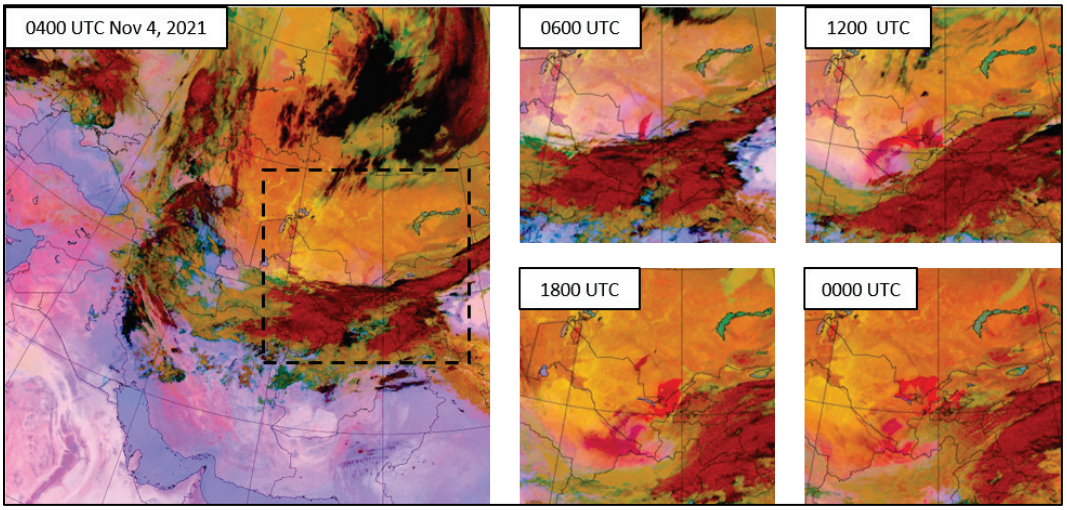

The Worldview imagery (Figure 27) displays a clear picture of the dust event that began around 0600 UTC on 4 November. A large cloud shield marked the southern edge of the anticyclone, while the accompanying cold front and 870 hPa inversion layer (e.g., Figure 26) held the air mass in place. In the 1200 UTC image in Figure 26, the coverage of the dust plume spread substantially, but it appeared to remain trapped by the surrounding mountainous terrain.

Figure 27. Worldview true-color imagery from (*top*) 4 November and (*bottom*) 5 November.

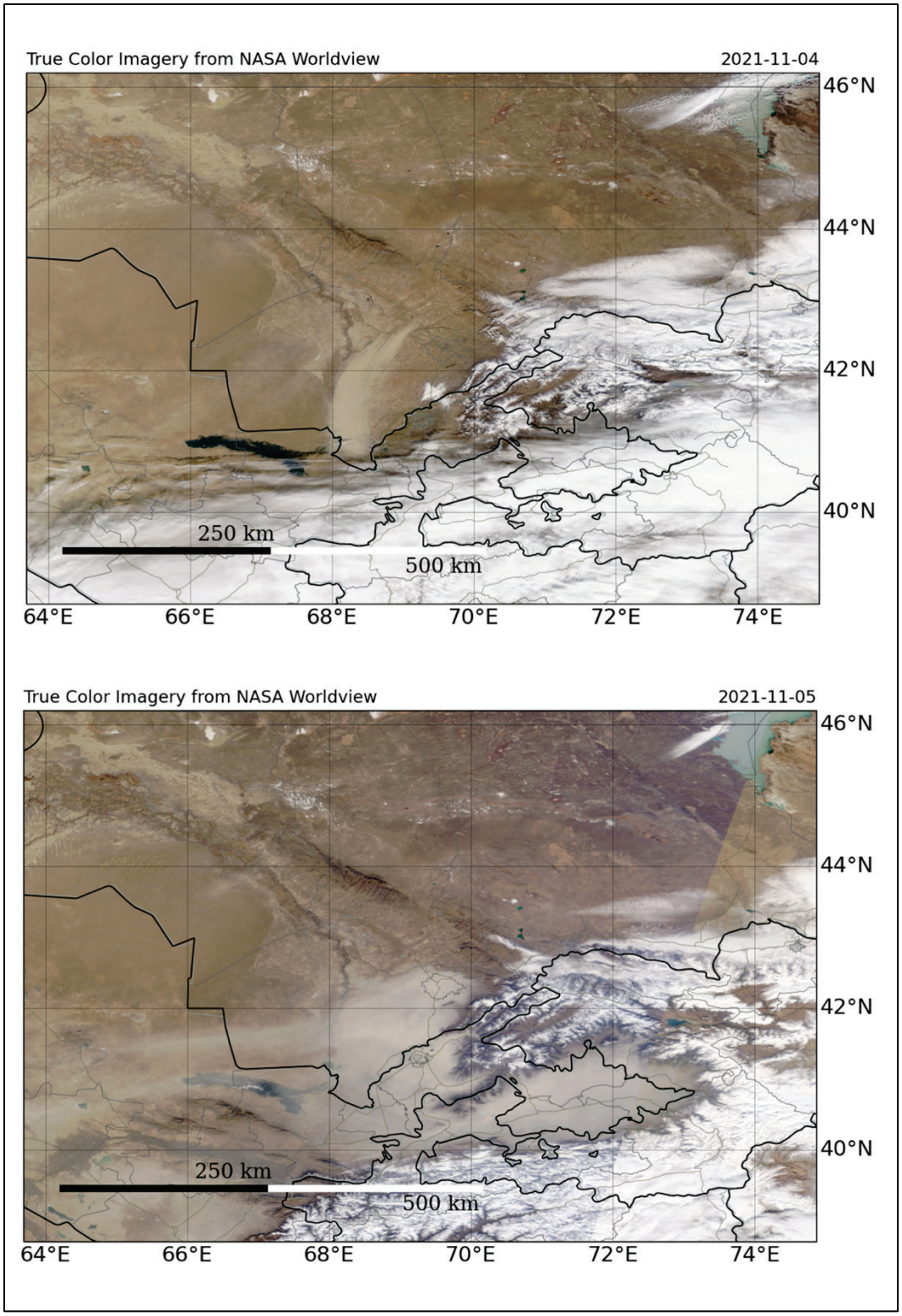

The HYSPLIT simulation of this event showed the tracer particles originating from an assumed dust source at 41.10°N 67.63°E (Figure 28). Particles

dispersed along a southward trajectory until the Hissar and Alay Mountains halted the plume's southward progress (Figure 28*a*–*b*). From that point forward, the tracers dispersed in all directions, with a plume favoring the eastward advection of particles into the Fergana Valley (Figure 28*c*–*d*). This analysis illustrated the topographic interactions that helped shape this event's evolution.

Figure 28. Worldview imagery for 5 November 2021. *Red markers* show the locations of particles released by the HYSPLIT model at a point location near the dust source along the border of Kazakhstan and Uzbekistan at different times throughout the event. The HYSPLIT model was initialized at 04 UTC (Z) on 4 November. The background image in this figure does not change, and the location of the HYSPLIT particles at the 24-hour time is roughly representative of the timing of the true-color image.

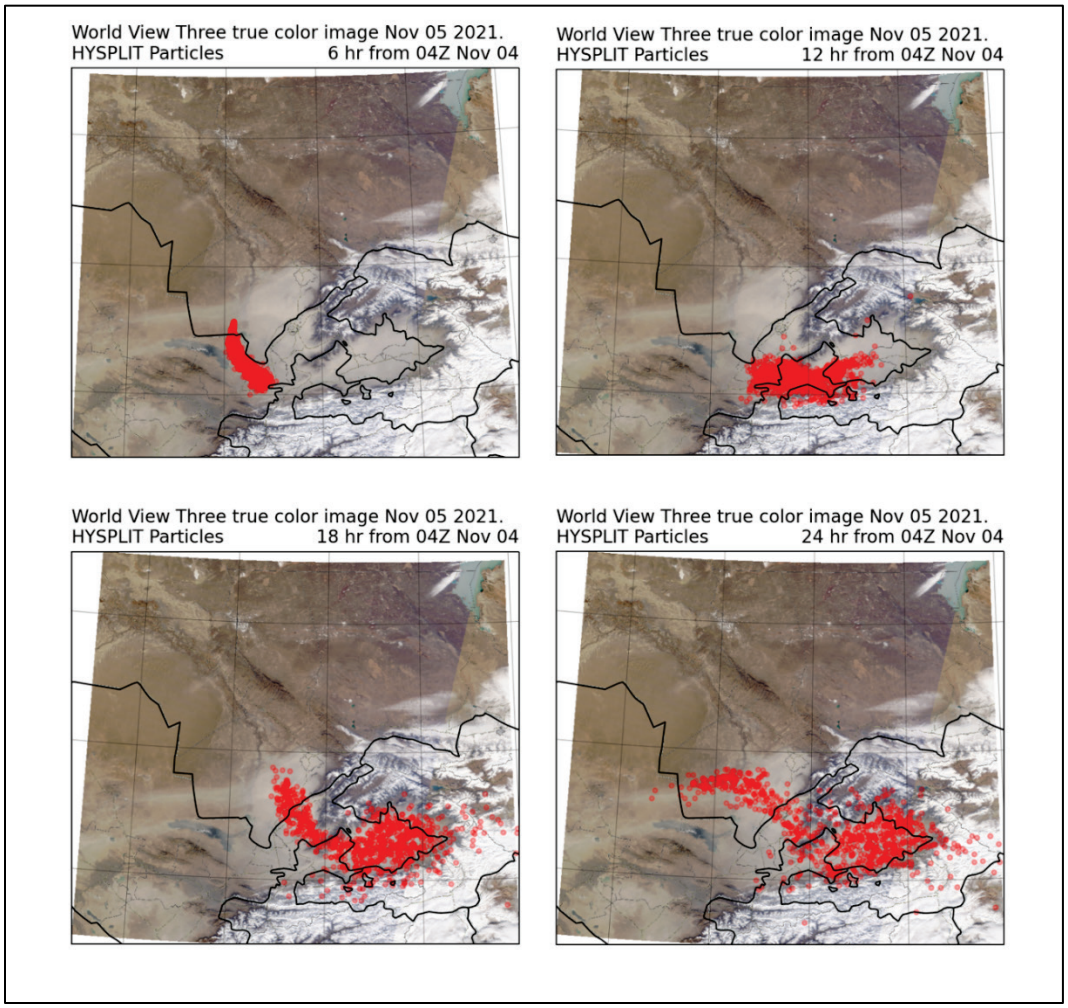

The CALIPSO profile transect data from 5 November captured an unobscured view of the dust plume through breaks in the cloud cover (Figures 29 and 30). The CALIPSO 532 nm AOD measurements show increased

values over the Fergana Valley region of eastern Uzbekistan, with a maximum AOD value of 1.74. The vertical profile of the 532 nm extinction coefficient shows most of the dust trapped below the approximately 850 hPa level, an outcome attributed to the previously discussed temperature inversion that occurred throughout the event. None of the other CALIPSO collections associated with this time frame provided additional insight for this event.

Figure 29. True-color imagery from Worldview with the CALIPSO 532 nm AOD. The *red markers* show the locations of radiosonde sites.

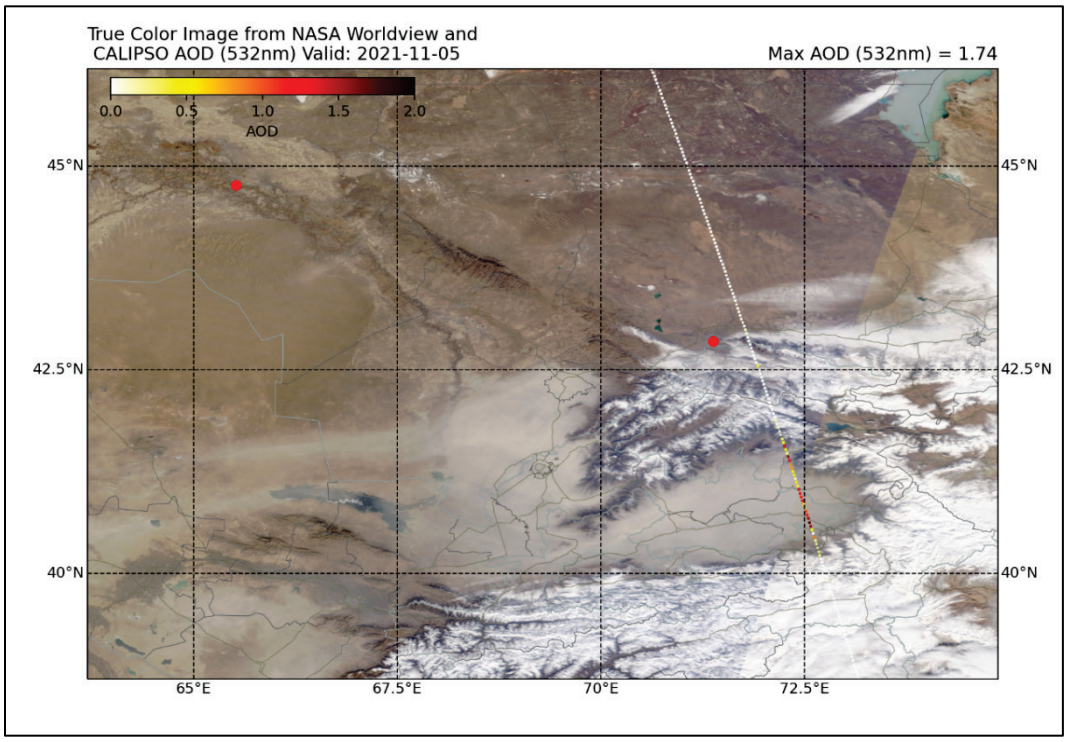

Figure 30. CALIPSO extinction coefficient vertical cross section from south to north (*color shaded*). The *solid-blue* shading indicates clouds. The *outlined gray surface* shows the approximate ground surface. (*Bottom*) Column-integrated AOD for the yellow-visible (535 nm) and NIR (1,064 nm). The main dust plume is between the 40°N to 42°N latitude bounds.

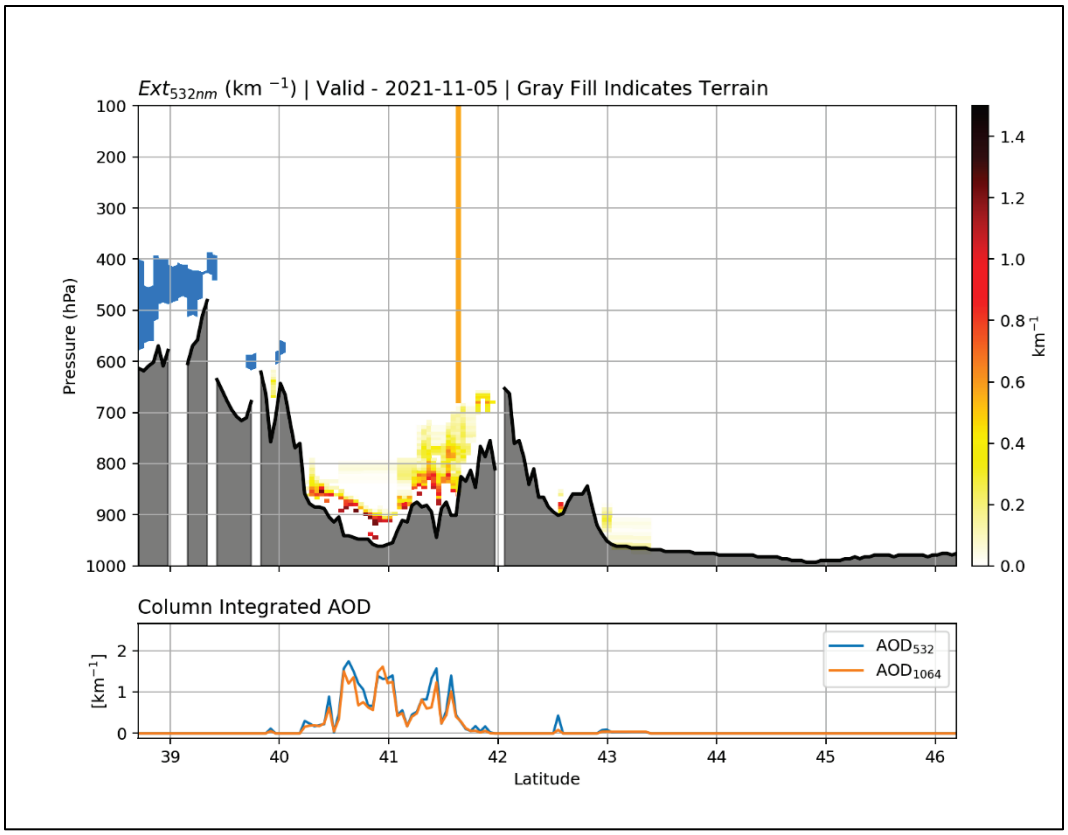

3.4 Central China, 2–7 May 2017

3.4.1 Event Overview

A deep midlatitude cyclone over the eastern part of Mongolia caused strong surface winds to develop over the Gobi Desert, between southern Mongolia and the Inner Mongolia Autonomous Region (IMAR). These winds created a large-scale dust event that affected more than 10 provinces of China and portions of the Korean Peninsula, Japan, and the northern Pacific Ocean (Figure 31). The prolonged dust event occurred from 2 to 7 May 2017. While the primary dust plumes associated with this event originated in the Gobi Desert, dust sourced from the Taklamakan Desert, the Hexi Corridor, and the Alxa Desert also contributed to the hazardous air quality conditions (Zhang et al. 2018). Worldview imagery captured the first dust plume on 2 May in conjunction with a strong surface low over parts of eastern Mongolia and northeastern China. The dust became widespread across much of China and Mongolia from 3 to 5 May,

with the southern and western regions of the IMAR experiencing the densest dust plumes over the event duration. According to Zhang et al. (2018), the widespread nature of this dust storm and the adverse effects it created in China, Korea, Japan, and the northern Pacific Ocean were highly unusual. The midlatitude cyclone eventually transported the dust out over the Pacific Ocean as it moved off the East Asia coastline on 7 May.

Figure 31. A map showing the general AOI for the 2–7 May 2017 event case study. The *red box* shows the general region in which dust emission was widespread. (Map image is the intellectual property of Esri and is used herein under license. Copyright 2020 Esri and its licensors. All rights reserved.)

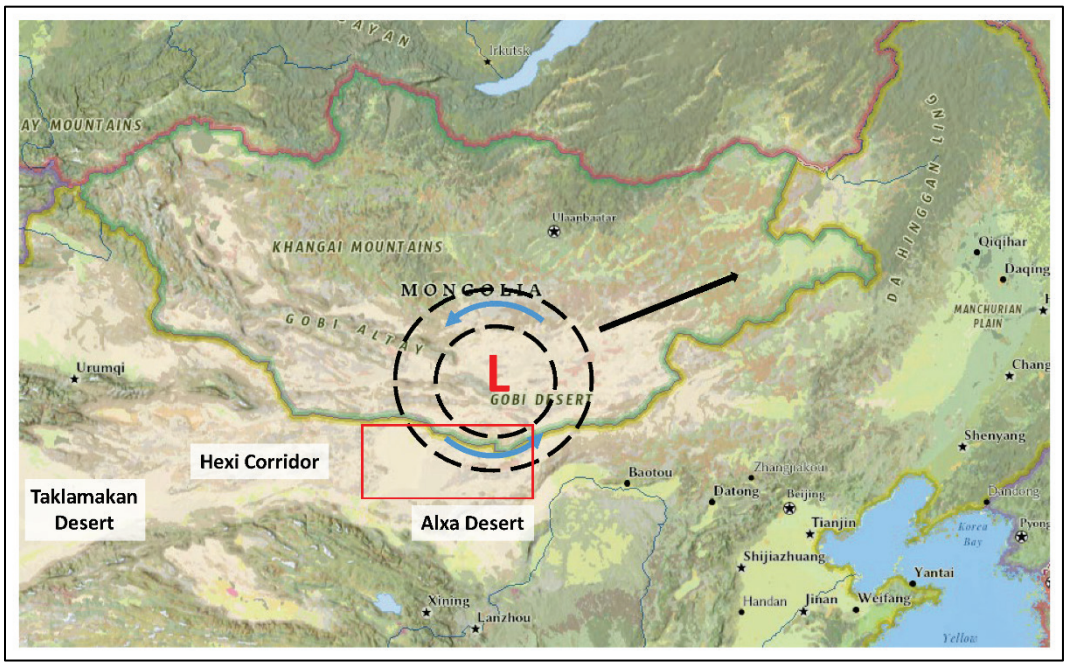

3.4.2 Synoptic Overview

A highly amplified upper-level trough and the development of a strong midlatitude cyclone shaped the synoptic setup for this event. Prior to the initiation of the dust event, the 0000 UTC 300 hPa ERA5 analysis of wind speed and heights displayed a positively tilted trough located over central Russia, with the base of the trough axis extending into northeastern Kazakhstan (Figure 32*a*). Two embedded jet streaks were present at the entrance and exit regions of the trough, where winds exceeded 70 m s^{-1}. Two secondary short-wave troughs, associated with the large-scale trough pattern over the area, were present over Central and Western China. Two secondary jet streaks were also occurring in the waves over Central China, where maximum 300 hPa winds were exceeding 50 m s^{-1} in some areas. By 2 May, the trough had advanced eastward with an increase in 300 hPa

wind speed in the exit regions of the jet streaks over Central China (Figure 32*b*). By 3 May, an upper-level *diffluence* zone developed within the exit region of the trough, with jet streak winds reaching speeds of 75 m s^{-1}. At this time, the trough had also become negatively tilted, and the upper-level jet dynamics were conducive for rapid cyclogenesis east of the trough axis. The trough moved slowly eastward on 3–6 May, with continuous, strong upper-level jet streak winds persisting over areas within Central and Northeast China (Figure 32*c*–*f*). By 0000 UTC on 6 May, the trough was moving off the mainland of China over the western Pacific Ocean. A broad upper-level high pressure ridge moved in behind the trough over portions of northern China and much of Mongolia, while another upper-level short-wave trough developed to the south over Central and southern China. The pattern supporting the midlatitude cyclone over this region had exited to the east by 0000 UTC on 7 May.

Figure 32. The 300 hPa heights and winds illustrating the upper-level dynamics at various times ahead of and during the event.

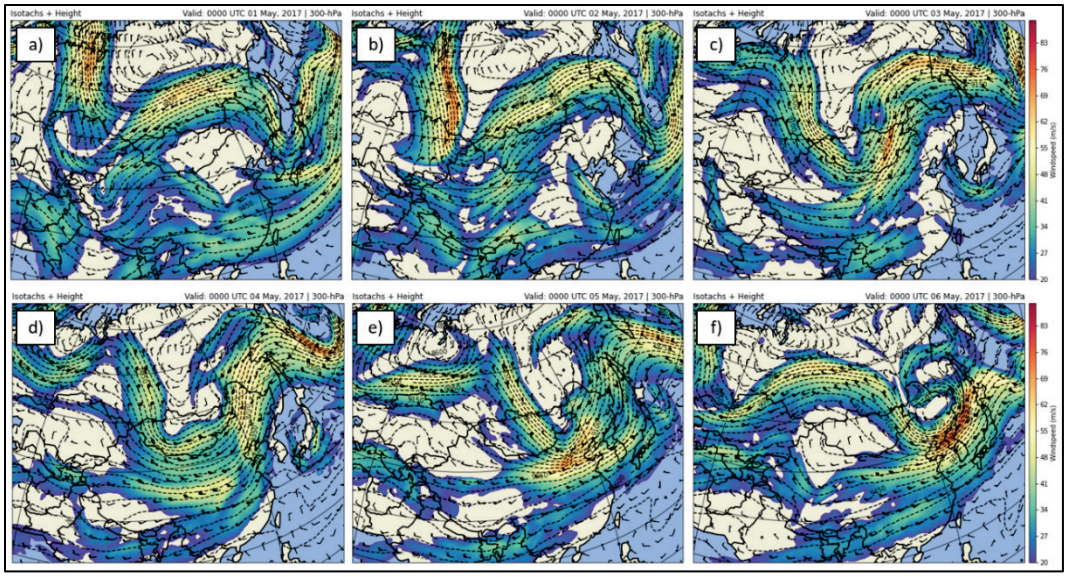

In the 850 hPa ERA5 analysis from 0000 UTC on 1 May, a frontal boundary extended over the Tian Shan Mountains, just north of the Taklamakan Desert (Figure 33*a*). The MSLP ERA5 analysis from the same time period also showed winds along the front reaching speeds >15 m s^{-1} (Figure 33*b*). On 2 May, cooler air continued to advect southward into parts of Western China, while low-level cyclogenesis was occurring over eastern Mongolia. This environmental setup led to a prolonged period of strong surface winds and dust lofting over the Gobi Desert in the following days.

Figure 33. (*a*) The 850 hPa temperature and heights and (*b*) MSLP and 10 m wind speed for 00 UTC on 1 May 2017. The *red oval* highlights the strong winds over the dust source region.

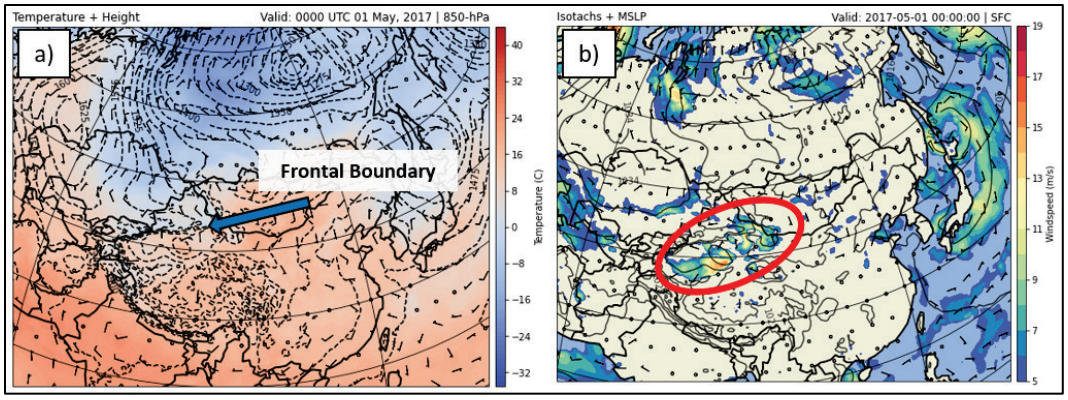

At 0000 UTC on 3 May, the 850 hPa ERA5 analysis indicated that the cold front had swept across much of Mongolia and portions of northern China (Figure 34*a*). A strong frontal boundary was near the border of Northeast China and Mongolia, along with a deep surface low. The very clear separation of the warm sector and cold sector of the midlatitude cyclone was indicative of an intensifying cyclone. The 0000 UTC MSLP ERA5 analysis for 3 May displayed strong surface winds associated with the intensifying midlatitude cyclone occurring over the Gobi Desert (Figure 35*a*). Winds over this dust-source region were in excess of 15 m s^{-1} at the time, which was favorable for entraining and transporting dust aerosols. The storm continued to intensify and remained nearly stationary between 3 and 4 May, with the MSLP reaching a minimum pressure of 986 hPa (Figure 35*c*). The strongest area of surface winds, approaching 19 m s^{-1}, moved along the border of Mongolia until the midlatitude cyclone began to exit the region on 6 May. These enhanced winds occurred in conjunction with the northeastward propagating frontal boundary visible on the 850 hPa ERA5 analysis. By 7 May, the surface winds had subsided over inland China, with the strongest winds within the warm sector of the midlatitude cyclone over the western Pacific Ocean.

Figure 34. The 850 hPa temperature and height analysis for 00 UTC on 3–6 May 2017.

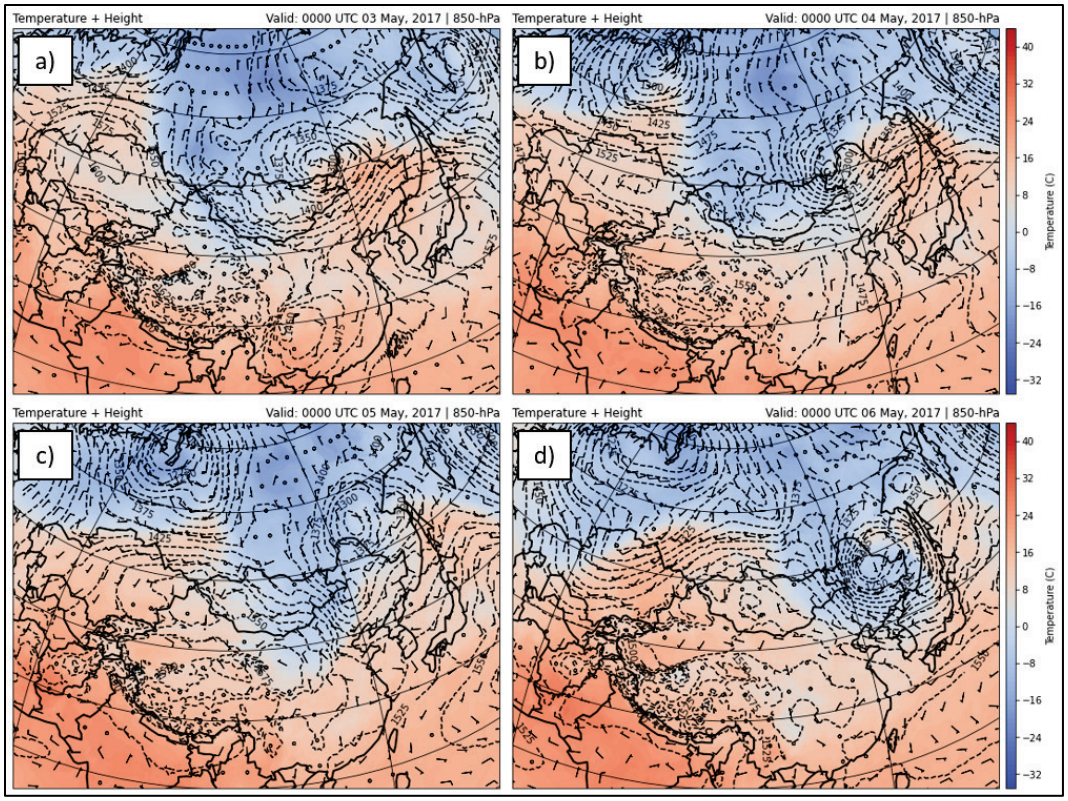

Figure 35. MSLP and wind speed analysis for 00 UTC on 3–6 May 2017.

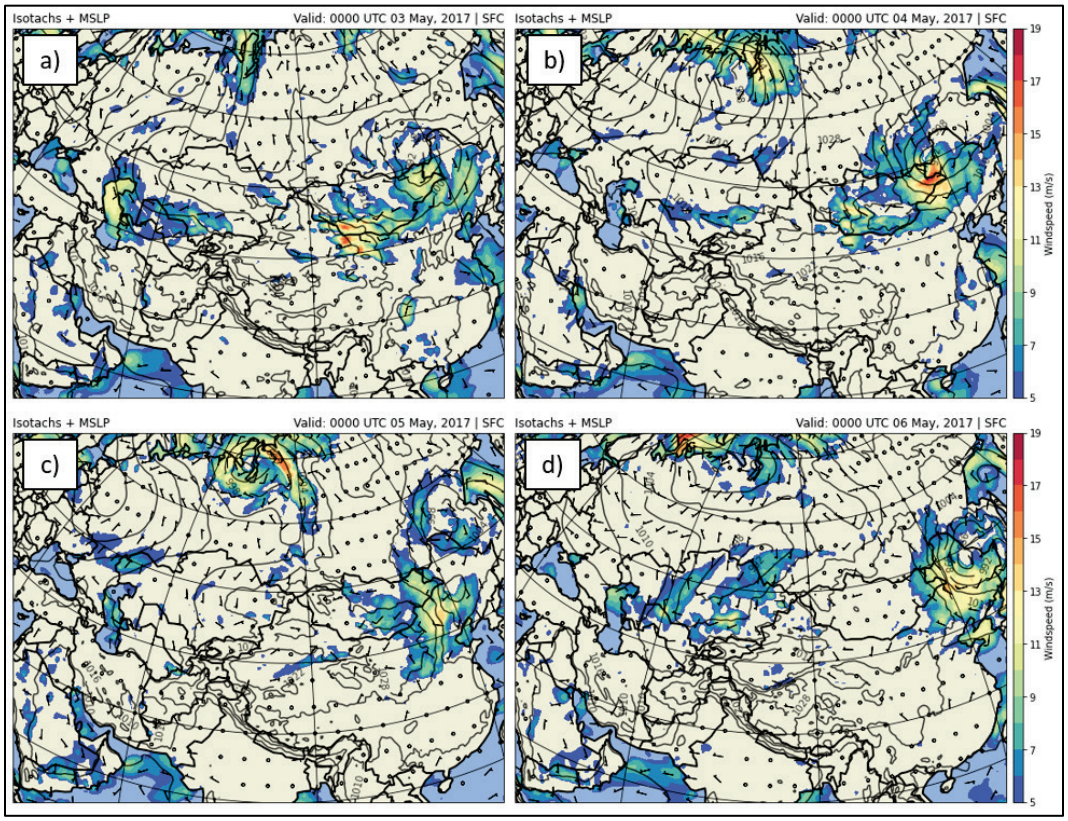

In summary, this event resulted from a deep midlatitude cyclone, with a collocated surface low, that influenced strong surface winds over the Gobi Desert. For a numerical weather model to accurately represent the event, it would need to reproduce the timing and placement of the highly amplified upper-level trough that propagated across the region between 1 and 7 May. The simulation would need to recreate the rapid cyclogenesis that occurred east of the trough axis, which led to strong surface winds developing over the Gobi Desert.

3.4.3 Dust Event Overview

The limited availability of archived MSG-SEVIRI data from 2017 and the presence of cloud cover in the Worldview imagery made it difficult to assess the evolution of the dust transport associated with this event. However, dense dust was visible in the satellite imagery beginning on 3 May in the Gobi Desert region (e.g., Figure 36). There also appeared to be dust extending to areas north of Beijing as dust was quickly transported eastward by the strong wind dynamics (surface winds >15 m s^{-1}) associated with this system as the surface low strengthened over the border of eastern Mongolia and northeastern China. On 4 May, the dust plume became more widespread, with dust wrapping around the midlatitude cyclone in a comma-shaped pattern (Figure 37). At this time, dust extended from the Gobi Desert across Beijing, IMAR, and far northeastern China. On 5–6 May, dust was still present on Worldview imagery, extending from areas near Beijing to the Sea of Japan. The dust also appeared to extend across the border of China into portions of Russia, where the cyclonic flow was wrapping the dust around the midlatitude cyclone the previous day. The coverage of dust continued to be widespread over far eastern portions of China to the western Pacific Ocean on 6 May before clearing out on 7 May. Worldview imagery was available for the initial dust emission event occurring on 2 May over the Gobi Desert.

The AOD transects collected by the CALIPSO sensor captured the dust storm in progress, providing more detailed information about the vertical distribution of dust for 3–4 May. On 3 May, the CALIPSO sensor intermittently sampled the downstream edge of the main dust plumes between cloud cover gaps (AOD values for the 532 nm wavelength [AOD_{532}] generally ranged between 1.0 and 2.0 in the dusty areas) and recorded a maximum AOD_{532} of 2.28 in southern Mongolia (Figures 36 and 38). The vertical profile of the 532 nm extinction coefficient suggested that the dust plume extended throughout much of the 700 hPa atmospheric pressure

level (Figure 38). Another CALIPSO transect from 3 May captured a spike in AOD near the origin of the dust plumes over the Gobi Desert (Figures 36 and 39), with a maximum AOD value of approximately 2.15 sampled along the transect path near the southern Mongolian border. The vertical profiles of the 532 nm extinction coefficient associated with this second transect from 3 May also showed intermittent sampling of dust between cloud cover (Figure 39), suggesting high concentrations of dust near the land surface around 43°N, near the origins of the main dust plume. On 4 May, the CALIPSO sensor recorded extreme AOD conditions over northern China as it passed over the wake of the main dust plume (e.g., Figures 37 and 40). The transect included multiple AOD values >2.0 just south of the Mongolian border. The 532 nm extinction coefficient profile showed the vertical distribution of dust in the wake of the main dust event (e.g., Figure 40), suggesting that by 4 May, the dust had become well mixed in atmosphere, with the plume's vertical extent nearing 600 hPa.

Figure 36. True-color imagery from NASA Worldview with the CALIPSO AOD overlaid for two overpasses that occurred on 3 May 2017. The *letters* correspond to the transect labels used in Figures 38 and 39.

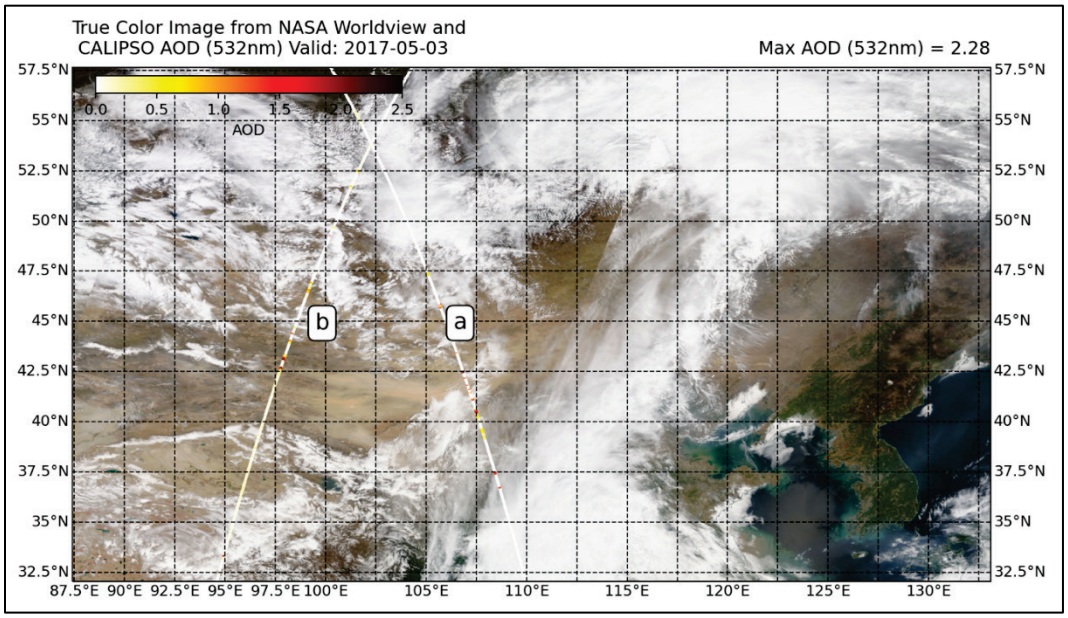

Figure 37. True-color imagery from NASA Worldview with the CALIPSO AOD overlaid for one overpass that occurred on 4 May 2017.

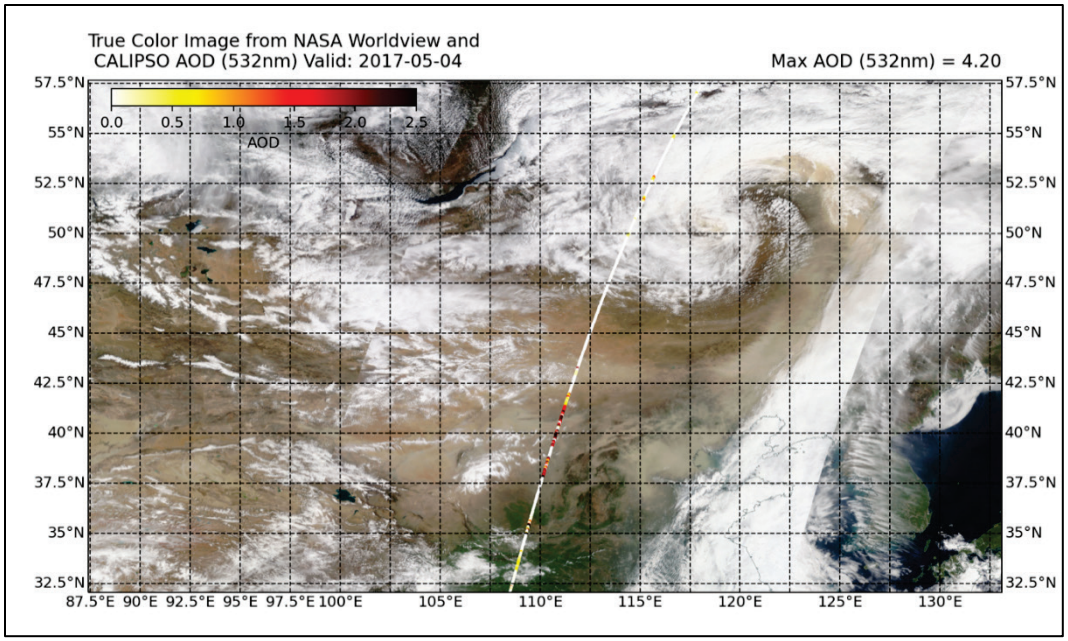

Figure 38. (*Top*) CALIPSO extinction coefficient vertical cross section from south to north (*color shaded*). The *solid-blue shading* indicates cloud. The *outlined gray surface* shows the approximate ground surface. (*Bottom*) Column-integrated AOD for the yellow-visible (535 nm) and NIR (1,064 nm). The main dust plume is between the 38°N and 45°N latitude bounds.

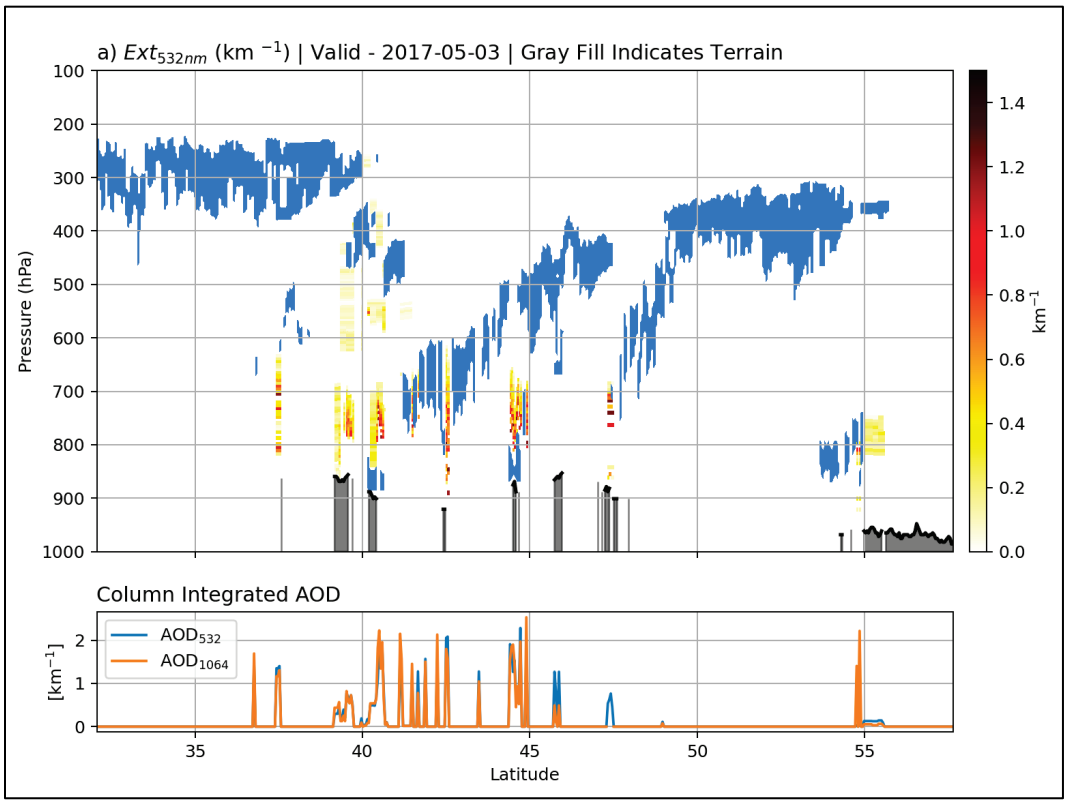

Figure 39. (*Top*) CALIPSO extinction coefficient vertical cross section from south to north (*color shaded*). The *solid-blue shading* indicates clouds. The *outlined gray surface* shows the approximate ground surface. (*Bottom*) Column-integrated AOD for the yellow-visible (535 nm) and NIR (1,064 nm). The main dust plume is between the 43°N and 45°N latitude bounds.

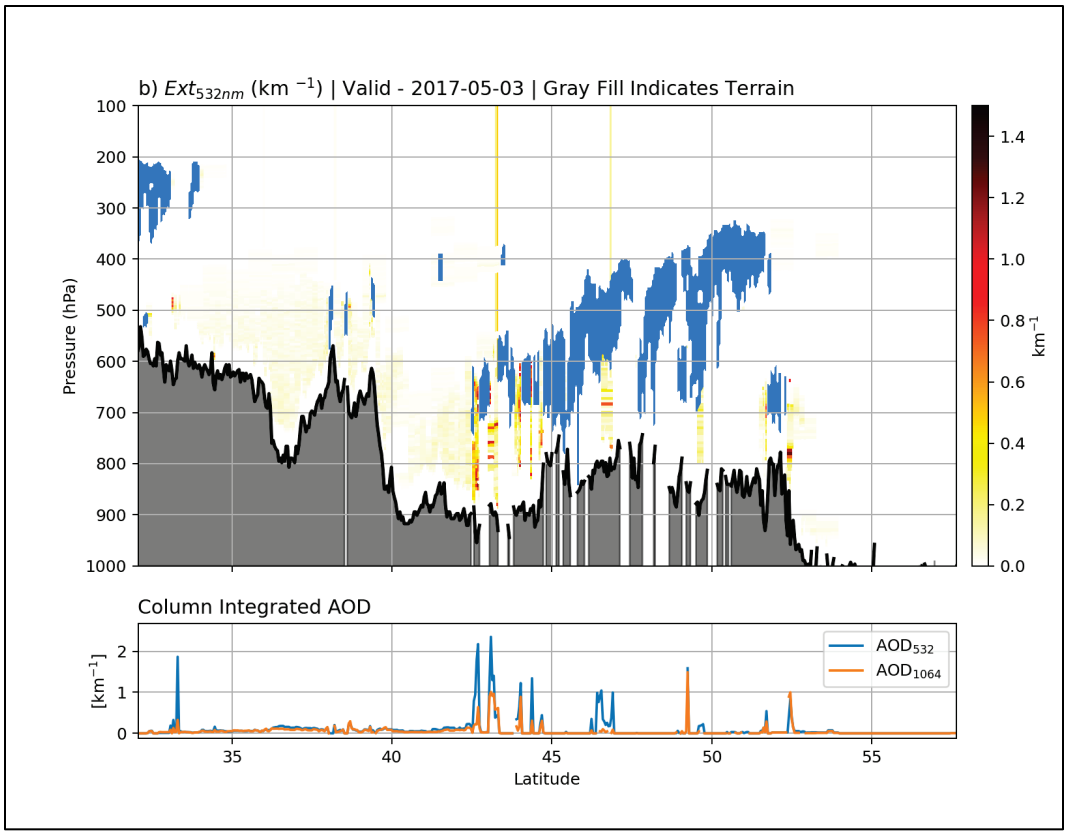

Figure 40. (*Top*) CALIPSO extinction coefficient vertical cross section from north to south (*color shaded*). The *solid-blue shading* indicates clouds. The *outlined gray surface* shows the approximate ground surface. (*Bottom*) Column-integrated AOD for the yellow-visible (535 nm) and NIR (1,064 nm). The main dust plume is between the 36°N and 46°N latitude bounds.

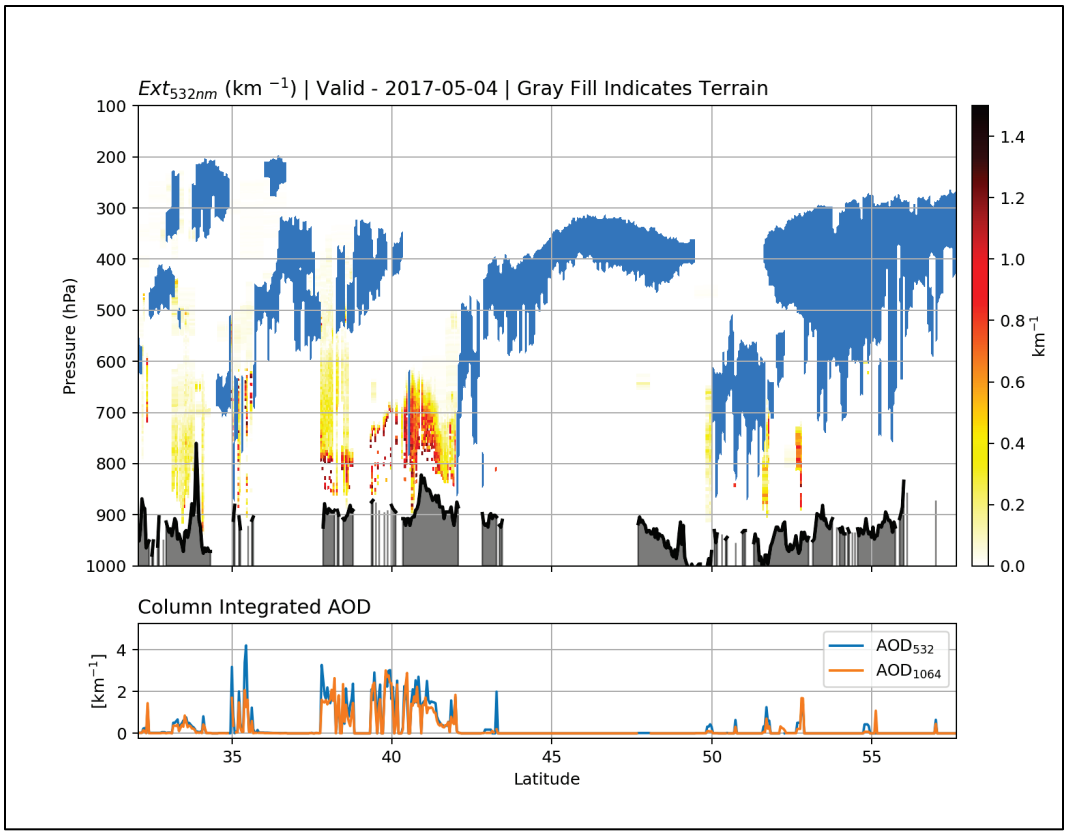

The HYSPLIT simulation for this event showed a steady plume of particles originating from a prescribed dust source at 40.99°N 103.23°E that generally matched the dust plumes visible in Figure 36 at the beginning of this event (Figure 41*a*). As time progressed, the particles became increasingly distributed along an elongated north-south transect following the cold front associated with the cyclone (Figure 41*a*–*c*). Approximately 24 hours after the event started, the particles were widespread across eastern China and broadly matched the dust visible in the true color imagery (Figure 41*d*).

Figure 41. Worldview imagery for 4 May 2017. *Red markers* show the locations of particles released by the HYSPLIT model at a point location near the dust source in northern China at different times throughout the event. The HYSPLIT model was initialized at 00 UTC (Z) on 3 May. The background image in this figure does not change, and the location of the HYSPLIT particles at the 24-hour time is roughly representative of the timing of the true-color image.

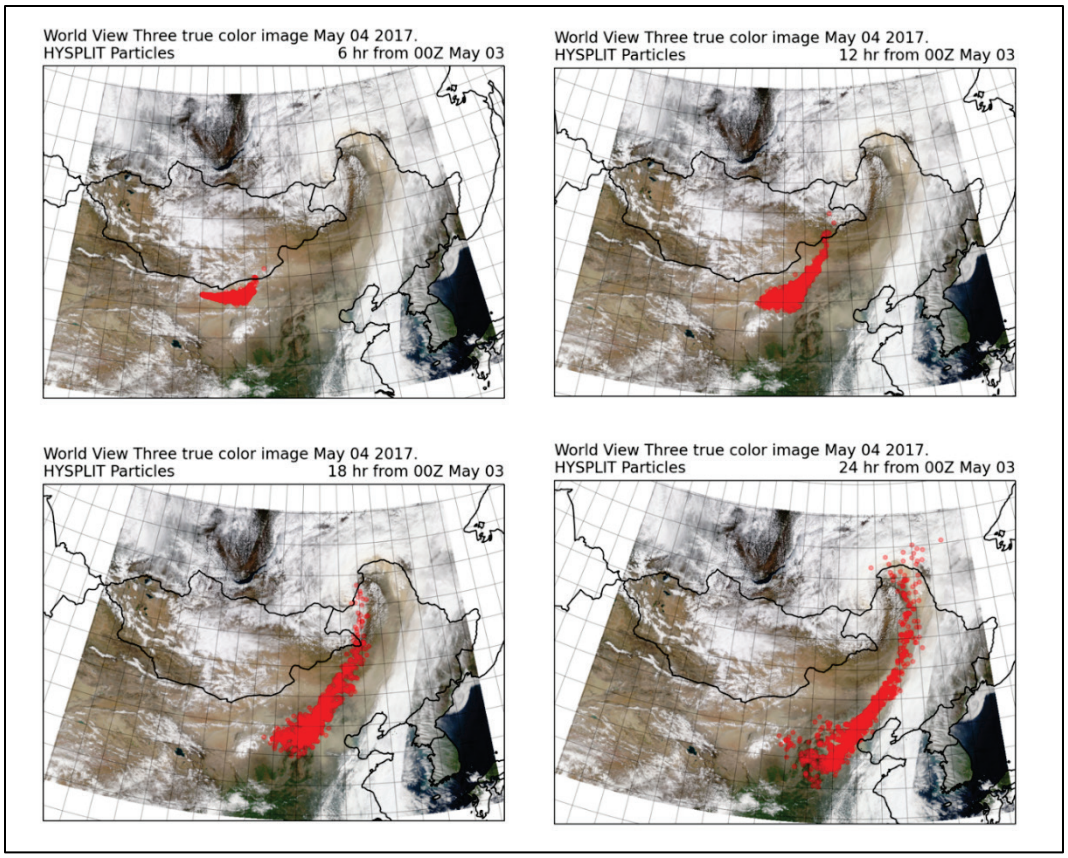

In summary, this was a large-scale, multiday (1–7 May) event that resulted from surface cyclogenesis occurring in conjunction with a midlatitude cyclone. Winds in the dust source region exceeded 15 m s^{-1} according to ERA5 reanalysis data. The strong surface winds lofted dust from the Gobi Desert and transported the emitted dust in a northeastward direction (e.g., Figure 41). After slow movement over the area, the midlatitude cyclone exited the region on 6 May, marking the end of the event. By 7 May, the strong surface winds had subsided, and the lingering plume of airborne dust had transported out of the area.

4 Conclusion

We analyzed four dust storm events that occurred across Central and East Asia. These four cases were selected from an inventory of potential events acquired from previous literature, news articles, and social media, and we prioritized them based on geographic location, forcing conditions, data availability, and societal impacts. For each of the focus case studies, we described the meteorological conditions, from the large-scale synoptic drivers to mesoscale and terrain influences, that controlled the dust event evolution. We also used HYSPLIT modeling techniques to supplement our analyses, which was especially important in the otherwise data-sparse regions.

Our analysis revealed that, while there were commonalities across our four focus events, each event exhibited unique aspects. For instance, terrain likely played an important role in amplifying the driving winds at the surface in the 13–20 March 2021 and the 4–5 November 2021 events. Additionally, analysis of each event illustrated that extreme dust storms are a result of multivariate processes involving a combination of fortuitous factors, including the meteorological drivers, soil erodibility, mesoscale wind variations, terrain, and even antecedent snow-cover and soil-moisture anomalies. This outcome indicates that accurately simulating all of these different factors is a prerequisite for an accurate dust transport and air quality simulation in the Central and East Asia regions.

We anticipate that the case study reference material provided in this report will support future numerical weather model validation efforts over Central and East Asia. However, we also encourage broader use of our findings as reference case studies for research focused on dust and air quality modeling.

References

Alter, R. E., S. L. LeGrand, F. D. Spates, W. D. Ledbetter, S. D. Minnigan, J. W. Thompson, K. I. Carter, and P. D. Elliott. 2022. *Meteorological Influence of a Major Dust Storm in Southwest Asia during July–August 2018*. ERDC TR-22-22. Vicksburg, MS: US Army Engineer Research and Development Center. http://dx.doi.org/10.21079/11681/45960.

AMS (American Meteorological Society). n.d. *Glossary of Meteorology* [Web edition]. Accessed August 30, 2021. http://glossary.ametsoc.org/wiki.

Baddock, M. C., C. L. Strong, P. S. Murray, and G. H. McTainsh. 2013. "Aeolian Dust as a Transport Hazard." *Atmospheric Environment* 71: 7–14. https://doi.org/10.1016/j.atmosenv.2013.01.042.

Banks, J. R., and H. E. Brindley. 2013. "Evaluation of MSG-SEVIRI Mineral Dust Retrieval Products over North Africa and the Middle East." *Remote Sensing of Environment* 128: 58–73. https://doi.org/10.1016/j.rse.2012.07.017.

Bao, C., M. Yong, C. Bueh, Y. Bao, E. Jin, Y. Bao, and G. Purevjav. 2022. "Analyses of the Dust Storm Sources, Affected Areas, and Moving Paths in Mongolia and China in Early Spring." *Remote Sensing* 14 (15): 3,661. https://doi.org/10.3390/rs14153661.

BBC News. 2021. "Sandstorm Swallows City in Northwestern China." *BBC News*, July 26, 2021. https://www.bbc.com/news/av/world-asia-china-57973810.

Brindley, H., P. Knippertz, C. Ryder, and I. Ashpole. 2012. "A Critical Evaluation of the Ability of the Spinning Enhanced Visible and Infrared Imager (SEVIRI) Thermal Infrared Red-Green-Blue Rendering to Identify Dust Events: Theoretical Analysis." *Journal of Geophysical Research: Atmospheres* 117 (D7): D07201. https://doi.org/10.1029/2011JD017326.

Center of the Hydrometeorological Service of the Republic of Uzbekistan. n.d. "Информация о несезонных явлениях пыльной мглы из-за сильных ветров [Information on Non-seasonal Dust Haze Events Due to Strong Wind]." *Uzhydromet*. Accessed June 28, 2022. https://hydromet.uz/ru/node/1039.

Chen, W., H. Meng, H. Song, and H. Zheng. 2022. "Progress in Dust Modelling, Global Dust Budgets, and Soil Organic Carbon Dynamics." *Land* 11 (2): 176. https://doi.org/10.3390/land11020176.

Department of the Army. 2019. *Intelligence Preparation of the Battlefield*. Army Techniques Publication (ATP) 2-01.3. Washington, DC: Headquarters, Department of the Army. https://armypubs.army.mil/epubs/DR_pubs/DR_a/ARN31379-ATP_2-01.3-001-WEB-4.pdf.

Department of the Army. 2020. *Army Aviation*. Field Manual 3-04. Washington, DC: Headquarters, Department of the Army. https://armypubs.army.mil/epubs/DR_pubs/DR_a/pdf/web/ARN21797_FM_3-04_FINAL_WEB_wfix.pdf.

Department of the Army. 2021. *Desert Operations*. Army Techniques Publication (ATP) 3-90.99. Washington, DC: Headquarters, Department of the Army. https://armypubs.army.mil/epubs/DR_pubs/DR_a/ARN32068-ATP_3-90.99-000-WEB-1.pdf.

Eurasianet. 2021. "Severe Dust Storm Engulfs Uzbekistan." *Eurasianet*, November 5, 2021. https://eurasianet.org/severe-dust-storm-engulfs-uzbekistan.

Filonchyk, M., and M. Peterson. 2022. "Development, Progression, and Impact on Urban Air Quality of the Dust Storm in Asia in March 15–18, 2021." *Urban Climate* 41: 101080. https://doi.org/10.1016/j.uclim.2021.101080.

Gallagher, A. R., S. L. LeGrand, T. S. Hodgdon, and T. W. Letcher. 2022. *Simulating Environmental Conditions for Southwest United States Convective Dust Storms Using the Weather Research and Forecasting Model v4.1*. ERDC TR-22-11. Vicksburg, MS: US Army Engineer Research and Development Center. http://dx.doi.org/10.21079/11681/44963.

Gonzalez-Martin, C., N. Teigell-Perez, B. Valladares, and D. W. Griffin. 2014. "The Global Dispersion of Pathogenic Microorganisms by Dust Storms and Its Relevance to Agriculture." *Advances in Agronomy* 127:1–41. https://doi.org/10.1016/B978-0-12-800131-8.00001-7.

Goudie, A. S., and N. J. Middleton. 2006. *Desert Dust in the Global System*. Berlin, Germany: Springer Berlin Heidelberg. https://doi.org/10.1007/3-540-32355-4.

Gui, K., W. Yao, H. Che, L. An, Y. Zheng, L. Li, H. Zhao, et al. 2022. "Record-Breaking Dust Loading During Two Mega Dust Storm Events over Northern China in March 2021: Aerosol Optical and Radiative Properties and Meteorological Drivers." *Atmospheric Chemistry and Physics* 22 (12): 7,905–7,932. https://doi.org/10.5194/acp-22-7905-2022.

Hall, D. K., and G. A. Riggs. 2021a. *MODIS/Terra Snow Cover Daily L3 Global 500m SIN Grid, Version 61* [Data set]. Boulder, CO: NASA National Snow and Ice Data Center Distributed Active Archive Center. https://doi.org/10.5067/MODIS/MOD10A1.061.

Hall, D. K., and G. A. Riggs. 2021b. *MODIS/Terra Snow Cover Monthly L3 Global 0.05Deg CMG, Version 61* [Data set]. Boulder, CO: NASA National Snow and Ice Data Center Distributed Active Archive Center. https://doi.org/10.5067/MODIS/MOD10CM.061.

He, Y., and F. Yi. 2015. "Dust Aerosols Detected Using a Ground-Based Polarization Lidar and CALIPSO over Wuhan (30.5° N, 114.4° E), China." *Advanced Meteorology* 2015: 536762. https://doi.org/10.1155/2015/536762.

Hersbach, H., B. Bell, P. Berrisford, S. Hirahara, A. Horányi, J. Muñoz-Sabater, J. Nicolas, et al. 2020. "The ERA5 Global Reanalysis." *Quarterly Journal of the Royal Meteorological Society* 146 (730): 1,999–2,049. https://doi.org/10.1002/qj.3803.

Huang, J., T. Wang, W. Wang, Z. Li, and H. Yan. 2014. "Climate Effects of Dust Aerosols Over East Asian Arid and Semiarid Regions." *Journal of Geophysical Research: Atmospheres* 119 (19): 11,398–11,416. https://doi.org/10.1002/2014JD021796.

Jin, J., M. Pang, A. Segers, W. Han, L. Fang, B. Li, H. Feng, H. X. Lin, and H. Liao. 2022. "Inverse Modeling of the 2021 Spring Super Dust Storms in East Asia." *Atmospheric Chemistry and Physics* 22: 6,393–6,410. https://doi.org/10.5194/acp-22-6393-2022.

Joint Chiefs of Staff. 2018. *Meteorological and Oceanographic Operations*. Joint Publication 3-59. Washington, DC: Joint Chiefs of Staff. https://www.jcs.mil/Portals/36/Documents/Doctrine/pubs/jp3_59.pdf.

Knippertz, P., and J.-B. W. Stuut. 2014. *Mineral Dust: A Key Player in the Earth System*. Dordrecht, Netherlands: Springer. https://doi.org/10.1007/978-94-017-8978-3.

LeGrand, S. L., and M. Brooks. 2018. *Sensitivity of Unified Model Dust Simulations to the ERDC-Geo Surface Erodibility Parameterization* [White paper]. Vicksburg, MS: US Army Corps of Engineers, Research and Development Center.

Liang, P., B. Chen, X. Yang, Q. Liu, A. Li, L. Mackenzie, and D. Zhang. 2021. "Revealing the Dust Transport Processes of the 2021 Mega Dust Storm Event in Northern China." *Science Bulletin (Beijing)* 67 (1): 21–24. https://doi.org/10.1016/j.scib.2021.08.014.

Liu, Y., J. R. Key, S. A. Ackerman, G. G. Mace, and Q. Zhang. 2012. "Arctic Cloud Macrophysical Characteristics from CloudSat and CALIPSO." *Remote Sensing of Environment* 124: 159–173. https://doi.org/10.1016/j.rse.2012.05.006.

Liu, Z., D. Liu, J. Huang, M. Vaughan, I. Uno, N. Sugimoto, C. Kittaka, et al. 2008. "Airborne Dust Distributions over the Tibetan Plateau and Surrounding Areas Derived from the First Year of CALIPSO Lidar Observations." *Atmospheric Chemistry and Physics* 8 (16): 5,045–5,060. https://doi.org/10.5194/acp-8-5045-2008.

Lott, N., R. Baldwin, and P. Jones. 2001. *The FCC Integrated Surface Hourly Database, A New Resource of Global Climate Data*. Technical Report 2001-01, Asheville, NC: US National Climate Data Center. https://repository.library.noaa.gov/view/noaa/13826/noaa_13826_DS1.pdf.

May, R. M., K. H. Goebbert, J. E. Thielen, J. R. Leeman, M. D. Camron, Z. Bruick, E. C. Bruning, et al. 2022. "MetPy: A Meteorological Python Library for Data Analysis and Visualization." *Bulletin of the American Meteorological Society* 103 (10): E2273–E2284. https://doi.org/10.1175/BAMS-D-21-0125.1.

MCST (MODIS Characterization Support Team). 2017. *MODIS 1km Calibrated Radiances Product* [Data set]. Greenbelt, MD: NASA MODIS Adaptive Processing System, Goddard Space Flight Center. http://dx.doi.org/10.5067/MODIS/MYD021KM.061.

Middleton, N. J. 2017. "Desert Dust Hazards: A Global Review." *Aeolian Research* 24: 53–63. https://doi.org/10.1016/j.aeolia.2016.12.001.

Miri, A., H. Ahmadi, M. R. Ekhtesasi, N. Panjehkeh, and A. Ghanbari. 2009. "Environmental and Socioeconomic Impacts of Dust Storms in Sistan Region, Iran." *International Journal of Environmental Studies* 66 (3): 343–55. https://doi.org/10.1080/00207230902720170.

NASA. n.d. *Worldview Version 4.2.0* [Web interface]. Accessed March 10, 2023. https://worldview.earthdata.nasa.gov.

National Centers for Environmental Information. 2018. *Federal Climate Complex Data Documentation for Integrated Surface Data (ISD)*. Asheville, NC: NOAA. https://www.ncei.noaa.gov/pub/data/noaa/isd-format-document.pdf.

National Centers for Environmental Information. n.d. *Index of /Pub/Data/NOAA* [Web archive]. Accessed March 10, 2023. https://www.ncei.noaa.gov/pub/data/noaa/.

Richter, D., and T. Gill. 2018. "Challenges and Opportunities in Atmospheric Dust Emission, Chemistry, and Transport." *Bulletin of the American Meteorological Society* 99 (7): ES115–ES118. https://doi.org/10.1175/BAMS-D-18-0007.1.

Rogowski, P., M. Otero, J. Hazard, T. Muschamp, S. Katz, and E. Terrill. 2021. "XMET—An Unattended Meteorological Sensing System for Austere Environments." *Journal of Atmospheric and Oceanic Technology* 38 (1): 17–30. https://doi.org/10.1175/JTECH-D-20-0016.1.

Rolph, G., A. Stein, and B. Stunder. 2017. "Real-Time Environmental Applications and Display sYstem: READY." *Environmental Modelling & Software* 95: 210–228. https://doi.org/10.1016/j.envsoft.2017.06.025.

Shepherd, G., E. Terradellas, A. Baklanov, U. Kang, W. A. Sprigg, S. Nickovic, A. D. Boloorani, et al. 2016. *Global Assessment of Sand and Dust Storms*. Nairobi, Kenya: United Nations Environment Programme. https://wesr.unep.org/redesign/media/docs/assessments/global_assessment_of_sand_and_dust_storms.pdf.

Sinclair, S. N., and S. L. Jones. 2017. *Subjective Mapping of Dust-Emission Sources by Using MODIS Imagery: Reproducibility Assessment*. ERDC/CRREL TR-17-8. Hanover, NH: US Army Engineer Research and Development Center, Cold Regions Research and Engineering Laboratory. http://dx.doi.org/10.21079/11681/22586.

Sinclair, S. N., and S. L. LeGrand. 2019. "Reproducibility Assessment and Uncertainty Quantification in Subjective Dust Source Mapping." *Aeolian Research* 40: 42–52. https://doi.org/10.1016/j.aeolia.2019.05.004.

Sparrow, K. H., and S. L. LeGrand. 2023. *Establishing a Series of Dust Event Case Studies for North Africa*. ERDC SR-23-1. Vicksburg, MS: US Army Engineer Research and Development Center. http://dx.doi.org/10.21079/11681/46445.

Sprigg, W. A., S. Nickovic, J. N. Galgiani, G. Pejanovic, S. Petkovic, M. Vujadinovic, A. Vukovic, et al. 2014. "Regional Dust Storm Modeling for Health Services: The Case of Valley Fever." *Aeolian Research* 14: 53–73. https://doi.org/10.1016/j.aeolia.2014.03.001.

Stein, A. F., R. R. Draxler, G. D. Rolph, B. J. B. Stunder, M. D. Cohen, and F. Ngan. 2015. "NOAA's HYSPLIT Atmospheric Transport and Dispersion Modeling System." *Bulletin of the American Meteorological Society* 96 (12): 2,059–2,077. https://doi.org/10.1175/BAMS-D-14-00110.1.

Tozer, P., and J. Leys. 2013. "Dust Storms—What Do They Really Cost?" *The Rangeland Journal* 35 (2): 131–142. https://doi.org/10.1071/RJ12085.

Tu, A., Z. Wang, Z. Wang, W. Zhang, C. Liu, X. Zhu, J. Li, et al. 2022. "Characterizing a Heavy Dust Storm Event in 2021: Transport, Optical Properties and Impact, Using Multi-Sensor Data Observed in Jinan, China." *Remote Sensing* 14 (15): 3,593. https://doi.org/10.3390/rs14153593.

University of Wyoming. n.d. *Department of Atmospheric Science* [Web archive]. Accessed November 15, 2022. http://weather.uwyo.edu/upperair/sounding.html.

Vergadi, E., G. Rouva, M. Angeli, and E. Galanakis. 2022. "Infectious Diseases Associated with Desert Dust Outbreaks: A Systematic Review." *International Journal of Environmental Research and Public Health* 19 (11): 6,907. https://doi.org/10.3390/ijerph19116907.

Walker, A. L., M. Liu, S. D. Miller, K. A. Richardson, and D. L. Westphal. 2009. "Development of a Dust Source Database for Mesoscale Forecasting in Southwest Asia." *Journal of Geophysical Research* 114: D18207. https://doi.org/10.1029/2008JD011541.

Watchers. 2021. "The Worst Dust Storm in Uzbekistan's Recorded History." *The Watchers*, November 9, 2021. https://watchers.news/2021/11/09/worst-dust-storm-uzbekistan-recorded-history-november-2021/.

Winker, D. M., W. H. Hunt, and M. J. McGill. 2007. "Initial Performance Assessment of CALIOP." *Geophysical Research Letters* 34 (19): L19803. https://doi.org/10.1029/2007GL030135.

Wolfe, R. E., G. Lin, M. Nishihama, K. P. Tewari, J. C. Tilton, and A. R. Isaacman. 2013. "Suomi NPP VIIRS Prelaunch and On-Orbit Geometric Calibration and Characterization." *Journal of Geophysical Research: Atmospheres* 118 (20): 11,508–11,521. https://doi.org/10.1002/jgrd.50873.

Yin, Z., Y. Wan, Y. Zhang, and H. Wang. 2022. "Why Super Sandstorm 2021 in North China?" *National Science Review* 9 (3): nwab165. https://doi.org/10.1093/nsr/nwab165.

Zhang, X.-X., B. Sharratt, L.-Y. Liu, Z.-F. Wang, X.-L. Pan, J.-Q. Lei, S.-X. Wu, et al. 2018. "East Asian Dust Storm in May 2017: Observations, Modelling, and its Influence on the Asia-Pacific Region." *Atmospheric Chemistry and Physics* 18 (11): 8,353–8,371. https://doi.org/10.5194/acp-18-8353-2018.

Zhao, A., C. L. Ryder, and L. J. Wilcox. 2022. "How Well Do the CMIP6 Models Simulate Dust Aerosols?" *Atmospheric Chemistry and Physics* 22 (3): 2,095–2,119. https://doi.org/10.5194/acp-22-2095-2022.

Zhou, C., H. Gui, J. Hu, H. Ke, Y. Wang, and X. Zhang. 2019. "Detection of New Dust Sources in Central/East Asia and their Impact on Simulations of a Severe Sand and Dust Storm." *Journal of Geophysical Research: Atmospheres* 124 (17–18), 10,232–10,247. https://doi.org/10.1029/2019JD030753.

Zilberman, A., and N. Kopeika. 2022. "A Simple Model for Assessing Millimeter-Wave Attenuation in Brownout Conditions." *Sensors* 22 (22): 8,889. https://doi.org/10.3390/s22228889.

Appendix: Technical Glossary of Meteorological Terms

This section provides descriptions of meteorology specific terminology as defined by the American Meteorological Society (AMS). Terms defined here are indicated throughout the report using an asterisk. The definitions here are in line with the definitions of these terms provided by the AMS (n.d.) Glossary of Meteorology website. For additional guidance on meteorological terminology, we recommend readers review the AMS glossary.

Aerosol optical depth (AOD)—A dimensionless product that integrates the radiative extinction coefficient (β_{ext}) throughout a specific atmospheric depth.

$$AOD = \int_{z_1}^{z_2} \beta_{ext,} dz$$

AOD essentially quantifies how opaque the atmosphere is at a specified wavelength.

Barrier jet—A jet that forms in the lower atmosphere in response to a mountain ridge blocking the impinging flow. Barrier jets blow parallel to the mountain ridge orientation due to Coriolis and pressure gradient forces.

Convection—In general, convection describes the transport of heat and other fluid properties via both mechanical and buoyancy driven fluid mixing. In the context of this report, convection refers to buoyancy driven motion within the atmosphere and its associated weather phenomena.

Cyclogenesis—The development of strengthening of a midlatitude cyclone. Cyclogenesis is marked by a drop in mean sea-level pressure (MSLP) at the surface and the development of synoptic scale cyclonic flow around the low-pressure center.

Dewpoint—An absolute measure of moisture within the atmosphere. Specifically, this is the temperature at which an air parcel will become saturated if the air parcel is cooled at a constant pressure.

Diffluence—Rate that adjacent flow diverges along an axis oriented normal to the flow at a specific point. This is measured by the quotient of $\partial \mathrm{v_n}$ and $\partial \mathrm{n}$, where V is wind speed, n is the axis oriented at 90° clockwise from the direction wind vector, and v_n is the component of the wind in the n direction.

Divergence—In the context of meteorology, divergence describes the spreading out of the horizontal velocity field. Mathematically, it is taken as the dot product between the gradient operator ($\vec{\nabla}$) and the wind vector ($\vec{U}$):

$$Div = \vec{\nabla} \cdot \vec{U}.$$

Divergence in the upper troposphere is associated with rising motion and cyclogenesis at the surface. Conversely, divergence near the surface is associated with sinking motion throughout the atmospheric column and high pressure.

Equatorial entrance region—The region of a jet streak located on the equatorial (south in the northern hemisphere) side of the jet stream near the entrance of the jet streak. Atmospheric dynamics favor divergence in the upper troposphere as well as upward vertical velocity and cyclogenesis beneath this region.

Geopotential height—The height of a given point in the atmosphere relative to its potential energy per unit mass. Geopotential height is typically used in place of pressure to identify and track weather systems in the middle and upper troposphere.

Haboob—An intense dust storm that typically occurs in association with strong thunderstorm outflow boundaries or frontal passages. Haboobs have a dramatic and rapid onset, sharply reduce visibility to "brown out" conditions, and generally persist from minutes to hours. These aspects differentiate haboobs from other dust storms.

Jet streak—Relatively strong winds concentrated within the core of the upper-level jet stream.

Mesoscale—The scale that describes atmospheric phenomena that occurs with horizontal scales between 1 to 100s of kilometers. Typically, the

mesoscale refers to convective weather such as thunderstorms, mesoscale convective systems (MCS) and tropical cyclones, and terrain-driven winds such as mountain or sea breezes.

Mesoscale convective system (MCS)—A larger cluster of thunderstorms that acts as a unified weather system. MCSs are associated with broad areas of precipitation and winds. MCSs come in many different morphologies (e.g., squall lines) that have dynamic and kinematic features that extend beyond those of their constituent thunderstorms.

Radiosonde—A measurement of atmospheric conditions aloft using instrumentation attached to a weather balloon.

Ridge—In the context of meteorology, a ridge is used to describe an elongated region of high pressure that is typically identified as a poleward extension of higher geopotential height with anticyclonic winds following parallel to the curvature of the ridge.

Skew-T log-P diagram—A diagram that is used to analyze the atmospheric vertical profile of temperature, humidity, and winds. In this diagram, the log of pressure is plotted on the y-axis, and temperature (skewed by 45°) is plotted on the x-axis. Typically, data collected from a radiosonde is plotted using a skew-T log-p diagram. Many weather phenomena, including convective instability, can be diagnosed from a skew-T log-p diagram.

Synoptic scale—The scale that describes atmospheric phenomena that occurs on the 100s to 1,000s of kilometers. This typically includes surface high- and low-pressure systems, frontal boundaries, and mid tropospheric troughs and ridges.

Trough—The opposite of a ridge. In the context of meteorology, a trough describes an elongated region of lower pressure that is typically identified as an equatorward extension of lower geopotential height with cyclonic flow following the trough curvature.

Vorticity—A measure of the local rotation within a fluid, defined mathematically as the curl of the fluid flow (i.e., the cross product between the gradient operator ($\vec{\nabla}$) and the wind vector ($\vec{U}$):

$$\zeta = \vec{\nabla} \times \vec{U}.$$

Horizontal vorticity is often used to identify regions with strong cyclonic flow in the mid troposphere.

Abbreviations

AMS	American Meteorological Society
AOD	Aerosol optical depth
AOI	Area of interest
BBC	British Broadcasting Company
CALIOP	Cloud-Aerosol Lidar with Orthogonal Polarization
CALIPSO	Cloud-Aerosol Lidar and Infrared Pathfinder Satellite Observation
CAPE	Convective Available Potential Energy
CIN	Convective inhibition
ECMWF	European Center for Medium-Range Weather Forecasting
EL	Equilibrium level
ERDC	Engineer Research and Development Center
fSCA	Snow-covered area fraction
GFS-FNL	Global Forecast System model final analysis
HYSPLIT	Hybrid Single-Particle Lagrangian Integrated Trajectory
IMAR	Inner Mongolia Autonomous Region
ISD	Integrated Surface Database
LCL	Lifted condensation level
LFC	Level of free convection
LT	Local time
MCS	Mesoscale convective system

MODIS	Moderate Resolution Imaging Spectroradiometer
MSG	Meteosat Second Generation
MSG-SEVIRI	Meteosat Second Generation Spinning Enhanced Visible and InfraRed Imager
MSLP	Mean sea-level pressure
MUCAPE	Most unstable Convective Available Potential Energy
NIR	Near-infrared
PM_{10}	Particulate matter ≤10 μm in diameter
READY	Real-Time Environmental Applications and Display System
SCA	Snow-covered area
SEVIRI	Spinning Enhanced Visible InfraRed Imager
SRH	Storm relative helicity
U	Zonal; west to east
V	Meridional; south the north
VIIRS	Visible Infrared Imaging Radiometer Suite
Z	Zulu time

REPORT DOCUMENTATION PAGE

1. REPORT DATE	2. REPORT TYPE	3. DATES COVERED	
		START DATE	END DATE
October 2023	Final Special Report (SR)	FY22	FY23

4. TITLE AND SUBTITLE

Establishing a Series of Dust Event Case Studies for East Asia

5a. CONTRACT NUMBER	5b. GRANT NUMBER	5c. PROGRAM ELEMENT
5d. PROJECT NUMBER	**5e. TASK NUMBER**	**5f. WORK UNIT NUMBER**

6. AUTHOR(S)

Theodore W. Letcher, Kent H. Sparrow, and Sandra L. LeGrand

7. PERFORMING ORGANIZATION NAME(S) AND ADDRESS(ES)

See reverse.

8. PERFORMING ORGANIZATION REPORT NUMBER

ERDC SR-23-11

9. SPONSORING/MONITORING AGENCY NAME(S) AND ADDRESS(ES)	10. SPONSOR/MONITOR'S ACRONYM(S)	11. SPONSOR/MONITOR'S REPORT NUMBER(S)
Air Force Lifecycle Management Center 75 Vandenburg Drive, Building 1630 Hanscom AFB, MA 01731-2103	AFLCMC	

12. DISTRIBUTION/AVAILABILITY STATEMENT

Distribution Statement A. Approved for public release: distribution is unlimited.

13. SUPPLEMENTARY NOTES

MIPR F28DAN2070G001

14. ABSTRACT

Dust aerosols have a wide range of effects on air quality, health, land-management decisions, aircraft operations, and sensor data interpretations. Therefore, the accurate simulation of dust plume initiation and transport is a priority for operational weather centers. Recent advancements have improved the performance of dust prediction models, but substantial capability gaps remain when forecasting the specific location and timing of individual dust events, especially extreme dust outbreaks. Operational weather forecasters and US Army Engineer Research and Development Center (ERDC) researchers established a series of reference case study events to enhance dust transport model evaluation. These reference case studies support research to improve modeled dust simulations, including efforts to increase simulation accuracy on when and where dust is lofted off the ground, dust aerosols transport, and dust-induced adverse air quality issues create hazardous conditions downstream. Here, we provide detailed assessments of four dust events for Central and East Asia. We describe the dust-event lifecycle from onset to end (or when dust transports beyond the area of interest) and the synoptic and mesoscale environmental conditions governing the process. Analyses of hourly reanalysis data, spaceborne lidar and aerosol optical depth retrievals, upper-air soundings, true-color satellite imagery, and dust-enhanced false-color imagery supplement the discussions.

15. SUBJECT TERMS

Air quality; Climate; Computer simulation; Dust; Dust storms; East Asia; Geospatial data

16. SECURITY CLASSIFICATION OF:			17. LIMITATION OF ABSTRACT	18. NUMBER OF PAGES
a. REPORT	b. ABSTRACT	C. THIS PAGE		
Unclassified	Unclassified	Unclassified	SAR	81

19a. NAME OF RESPONSIBLE PERSON	19b. TELEPHONE NUMBER (include area code)

7. PERFORMING ORGANIZATION NAME(S) AND ADDRESS(ES) (concluded)

US Army Engineer Research and Development Center (ERDC)
Cold Regions Research and Engineering Laboratory (CRREL)
72 Lyme Road
Hanover, NH 03755-1290

US Army Engineer Research and Development Center (ERDC)
Geospatial Research Laboratory (GRL)
7701 Telegraph Road
Alexandra, VA 22315-3864